SUBSPACE ESTIMATION FOR SUBSPACE-BASED MAGNETIC RESONANCE SPECTROSCOPIC IMAGING

BY

BRYAN A. CLIFFORD

THESIS

Submitted in partial fulfillment of the requirements
for the degree of Master of Science in Electrical and Computer Engineering
in the Graduate College of the
University of Illinois at Urbana-Champaign, 2016

Urbana, Illinois

Adviser:

Professor Zhi-Pei Liang

ABSTRACT

Magnetic resonance spectroscopic imaging (MRSI) is a powerful technique that offers us the ability to non-invasively image chemical distributions within the human body. However, due to its inherently poor trade-off between imaging speed, resolution, and signal-to-noise ratio (SNR), MRSI has remained impractical for many research and clinical applications.

A large body of work has been done to improve this trade-off. Recently new subspace-based imaging methods have also been proposed as a means of dramatically accelerating MRSI. By taking advantage of the properties of a partially separable (PS) signal model, subspace-based methods offer increased flexibility in acquisition as well as image reconstruction, and thereby allow high-resolution, high-SNR MRSI images to be obtained in a fraction of the time required by standard techniques.

An important ingredient common to all subspace-based imaging methods is the estimation of the subspace structure of the high-dimensional image function. However, accurate subspace estimation in the presence of noise and inhomogeneity in the main magnetic field is challenging. To this end we propose a novel method for subspace estimation which utilizes a regularized-reconstruction approach to correct for the effects of field inhomogeneity and noise.

Carefully designed numerical simulations and experimental studies have been performed to evaluate the performance of the proposed method in a variety of experimental conditions. Results from these data show that the proposed method is able to obtain an accurate subspace estimation, either in terms of a projection error metric or by inspecting the residual after projecting the fully sampled data onto the estimated subspaces. Additionally, *in vivo* MRSI data was acquired to illustrate that the subspace estimated by the proposed method leads to high-quality spatiospectral reconstructions.

To my parents and friends, for their love and support.

ACKNOWLEDGMENTS

Since I was a child, I've always been interested in science and the how and why of things. I am so grateful to my parents for encouraging me in this line of pursuit. I know that it was not always easy for them, especially when I performed dangerous experiments in my room, the garage, and worst of all, in plain view of our concerned neighbors. One thing I know for sure is that without encouragement from parents, friends, and teachers I wouldn't have made it to graduate school.

Graduate school has not be easy for me, but it's not supposed to be. Since entering graduate school life has been a tough and grinding process, but I think a refining one. I've grown a lot both as a researcher and a person, and looking back I can see how my thought processes and problem solving skills have evolved to become more thorough and effective. In this aspect of my development, my advisor, Zhi-Pei, deserves a very large portion of the credit. I'm incredibly grateful for his advice, constructive criticism, and his patience.

I could never have reached this point in my career without the support and love from my family, friends, and labmates. I grateful very grateful for all of the advice, thoughtful discussions, and fruitful collaborations I've had with Drs. Fan Lam, Chao Ma, Anthony Christodoulou, Curtis Johnson, and Bo Zhao. I'd like to give a special thanks to Qiang Ning, Mohammed Sheikh, Yudu Li, Giang-Chau Ngo, Alex Cerjanic, Mao-Jin Fu, Ding Liu, Miguel Moscoso, and Qiegen Liu for their help and support. I'd also like to thank my best friends Yip, Matt, Brendon, Desiree, and Emily for their love and support.

TABLE OF CONTENTS

LIST OF ABBREVIATIONS

1D	One-Dimensional
2D	Two-Dimensional
3D	Three-Dimensional
ADC	Analogue to Digital Converter
CSI	Chemical Shift Imaging
Cho	Choline
Cr	Creatine
DFT	Discrete Fourier Transform
EPSI	Echo-Planar Spectroscopic Imaging
FID	Free Induction Decay
Glu	Glutamate
Gln	Glutamine
Glx	Glutamate and Glutamine
GRE	Gradient Echo
LVS	Linear Vector Space
MR	Magnetic Resonance
MRI	Magnetic Resonance Imaging
MRSI	Magnetic Resonance Spectroscopic Imaging
mI	myo-Inositol
NMR	Nuclear Magnetic Resonance

NMRS	Nuclear Magnetic Resonance Spectroscopy
NAA	N-AcetylAspartate
ppm	Parts-Per-Million
PRESS	Point RESolved Spectroscopy
PS	Partially Separable / Partial Separability
RF	Radio Frequency
SE	Spin Echo
SNR	Signal-to-Noise Ratio
SPICE	SPectroscopic Imaging by exploiting spatiospectral CorrElation
SVD	Singular Value Decomposition
UoS	Union-of-Subspaces

CHAPTER 1

INTRODUCTION

1.1 Motivation

Shortly after the first observation of nuclear magnetic resonance (NMR) in 1946 [1–3], NMR spectroscopy (NMRS) was developed and has since become an essential tool for chemical analysis due to the NMR signal's inherent dependence on both the chemical composition and molecular structure of the sample. The more recent technique of magnetic resonance spectroscopic imaging (MRSI) introduced by Lauterbur in 1975 [4] and pioneered in the early 1980s [5–8] uses spatial encoding methods to resolve the NMR signal into the signal contributions produced by localized regions of the sample. Because of its ability to estimate *in vivo* chemical distributions without the use of chemical tracers or ionizing radiation, MRSI has greatly influenced the biological fields. Studies in the field of neurology, for example, use MRSI to estimate the relative concentrations and distributions of brain metabolites, and attempt to correlate these measurements with various cancers [9–11] and neurological diseases such as Alzheimer's disease and multiple sclerosis [12, 13].

Unfortunately despite nearly four decades of development, current MRSI techniques are still far from reaching their potential. The inherently low intensity of the NMR signal creates a poor trade-off between imaging speed, resolution, and signal-to-noise-ratio (SNR), which has limited the utility of MRSI in many applications. Recently, new subspace-based methods for MRSI have been developed which provide dramatically better trade-offs and may pave the way toward fast, high SNR, and high-resolution MRSI [14–17]. A key aspect of these methods is the estimation of the spectral subspace of the MRSI spatiospectral distribution from data with low spatial resolution (limited spatial encodings). The goal of this thesis is to provide and analyze

a novel method for this estimation.

1.2 Main Results

- We formally define the MRSI subspace estimation problem in the framework of subspace-based imaging and propose a novel method for subspace estimation from a set of low-resolution, high-SNR data. A key challenge in this problem is the correction for inhomogeneities in the main magnetic field (B_0) of the magnetic resonance imaging (MRI) scanner. To this end we utilize regularization-based reconstruction methods to remove the effects of B_0 field inhomogeneities from the data prior to subspace estimation. We also introduce a metric for subspace estimation error and compare several different regularization terms based their abilities to provide reduced estimation errors.

- We test our method using both simulated and experimentally acquired data. A numerical phantom was generated using quantum mechanical simulations of brain metabolite spectra and used to create simulated data sets with varying levels of noise, resolution, and B_0 field inhomogeneity. Experimental data was acquired from a physical phantom containing brain metabolites at close to *in vivo* concentrations as well as a healthy human subject (with internal review board approval). Subspace estimation results using these data were confirmed the simulation-based results.

- We introduce novel methods for the selection of important parameters in our subspace estimation algorithm:

    1. We propose a method for the selection of the parameter associated with our weighted ℓ_2 difference regularization term from knowledge of the noise variance. Simulated data from our numerical phantom were used to show that the subspace estimation error obtained using this parameter is close to the minimum possible error obtained using this weighted ℓ_2 regularization method.
    2. Motivated by results in random matrix theory, we propose a method for the selection of the subspace dimension (or model order). Re-

sults from data generated from our numerical phantom showed that increasing the model order past the value produced by our method yielded little reduction in subspace estimation error.

1.3 Organization of the Thesis

This thesis is organized as follows:

Chapter 2 presents a review of the background material and concepts utilized in this thesis. In particular this chapter describes the generation and localization of the NMR signal as pertaining to MRSI. The challenges and standard approaches toward MRSI are also described.

Chapter 3 describes subspace-based MRSI and its applications. The mathematical concepts utilized by current subspace-based MRSI techniques as well as by this work are described in detail.

Chapter 4 defines the subspace estimation problem in the framework of subspace-based imaging and describes the theory behind our proposed method. The formulation of our regularized reconstruction schemes and our algorithms for solving them are described in detail. We also introduce and describe our methods for regularization parameter and model order selection.

Chapter 5 describes the analysis of our method through simulated and experimental results. Detailed descriptions of our simulations and experiments are described along with discussions of the results of our analyses.

Chapter 6 summarizes the conclusions of this study and briefly discusses future lines of research.

Lastly, the appendices provide derivations and algorithms mentioned in the body of the text.

CHAPTER 2

BACKGROUND

2.1 Magnetic Resonance Imaging

2.1.1 Signal Generation and Measurement

The fundamental property of matter responsible for the NMR signal is spin. Particles with non-zero spin (or spins) have an intrinsic magnetic dipole moment $\boldsymbol{\mu}$ with constant magnitude. In the absence of an external magnetic field the effect of the nuclear spins is negligible. However, when external magnetic fields are applied, coherent interactions of the nuclear spins with the fields result in observable effects. For a static, z-directed magnetic field $\boldsymbol{B}_0 = B_0\hat{\boldsymbol{z}}$, the energy of the interaction between a nuclear spin and the external field is given by

$$E = -\mu_z B_0, \tag{2.1}$$

where μ_z is the value of the z-component of $\boldsymbol{\mu}$. An important result from quantum mechanics is that μ_z can only take on quantized values (nuclear spin states), and therefore the values of E are also quantized. For half-spin nuclei the allowed values of μ_z are $\pm\gamma\!\!\!^{-}h/2$ where $\gamma\!\!\!^{-} := \gamma/2\pi$, γ is a nucleus dependent physical constant called the gyromagnetic ratio and h is Plank's constant. This "splitting" of nuclear energy levels due to the effect of the applied field (known as Zeeman splitting) is essential for the generation of the NMR signal. The effect leads to a difference (governed by the Boltzmann distribution) between the equilibrium numbers of nuclear spins with μ_z aligned parallel ($\mu_z = +\gamma\!\!\!^{-}h/2$) and anti-parallel ($\mu_z = -\gamma\!\!\!^{-}h/2$) to the applied field. The difference in the number of parallel and anti-parallel

spins can be approximated as [18]

$$\Delta N_{\pm} \approx N_s \frac{\gamma\!\!\!^{-} h B_0}{2KT_s}, \tag{2.2}$$

where N_s is the number of nuclear spins, K is the Boltzmann constant, and T_s is temperature of the spin system. This difference in equilibrium spin state populations leads to the generation of a macroscopic magnetic moment density called the bulk magnetization field ($\boldsymbol{M} = M_z^0 \hat{\boldsymbol{z}}$), the magnitude of which can be calculated as

$$M_z^0 = \frac{\Delta N_{\pm}}{\Delta V} \frac{\gamma\hbar}{2} = \rho_s \frac{\gamma\!\!\!^{-2} h^2 B_0}{4KT_s}, \tag{2.3}$$

where ΔV is the differential sample volume and $\rho_s := \frac{N_s}{\Delta V}$ is the spin population density.

The first step of a MRI experiment is the establishment of M_z^0 and is achieved by placing the sample inside the scanner which supplies a strong, uniform, static magnetic field $\boldsymbol{B}_0$. The second step is apply a time-varying magnetic field ($\boldsymbol{B}_1$), which is usually in the form of a radio frequency (RF) pulse called an excitation pulse. The effect of external magnetic fields on the time evolution of $\boldsymbol{M}$ is governed by a phenomenological equation called the *Bloch equation*

$$\frac{d\boldsymbol{M}}{dt} = \gamma \boldsymbol{M} \times \boldsymbol{B} - \frac{M_x \hat{\boldsymbol{x}} + M_y \hat{\boldsymbol{y}}}{T_2} - \frac{(M_z - M_z^0)\hat{\boldsymbol{z}}}{T_1}. \tag{2.4}$$

In this equation $\boldsymbol{B} = B_0 \hat{\boldsymbol{z}} + \boldsymbol{B}_1$, and M_x, M_y, and M_z represent the components of $\boldsymbol{M}$ along the different spatial axes. T_2 and T_1 are relaxation constants specifying how rapidly the transverse component ($\boldsymbol{M}_{xy} := M_x \hat{\boldsymbol{x}} + M_y \hat{\boldsymbol{y}}$) and longitudinal component (M_z) return to equilibrium ($\boldsymbol{M} = M_z^0 \hat{\boldsymbol{z}}$).

When the excitation pulse ends, there will be a transverse component which according to Eq. 2.4 will freely precess about the z-axis at the resonant frequency of the spin population

$$f_0 = \gamma\!\!\!^{-} B_0, \tag{2.5}$$

which is known as the *Larmor frequency*. The temporal variation of $\boldsymbol{M}$ is measured using a receiver coil and the signal induced in the coil is called a

free induction decay (FID). For time-harmonic signals at frequency f, the induced voltage in the coil (V) is governed by the following equation (see Appendix A.1)

$$V = -2\pi f \int_{V_{\text{sample}}} \boldsymbol{M} \cdot \boldsymbol{B}_r dv, \tag{2.6}$$

where $\boldsymbol{B}_r$ is referred to as the sensitivity profile and corresponds to the magnetic field that would be induced in the sample when unit current is applied to the receiver coil. Modern MRI scanners utilize quadrature detection [18] so the actual signal $s(t)$ recorded by the scanner can be written as

$$s(t) \propto 2\pi f_0 \int_{V_{\text{sample}}} M_{xy}(\boldsymbol{x}) B_{r,xy}(\boldsymbol{x}) e^{-t/T_2(\boldsymbol{x})} e^{-i2\pi \gamma \Delta B_0(\boldsymbol{x}) t} d\boldsymbol{x}, \tag{2.7}$$

where $M_{xy} := M_x + iM_y$, $B_{r,xy} := B_{r,x} + iB_{r,y}$ and $\Delta B_0(\boldsymbol{x})$ is inhomogeneity in the main magnetic field at a given location $\boldsymbol{x}$. Note that we have also assumed that T_2 is much larger than $1/f_0$.

The term $M_{xy}(\boldsymbol{x}) B_{r,xy}(\boldsymbol{x})$ and proportionality constants are usually combined and referred to as the *spin density*. Denoting the spin density as $\rho(\boldsymbol{x})$ the Eq. (2.7) can be written as

$$s(t) = \int_{V_{\text{sample}}} \rho(\boldsymbol{x}) e^{-t/T_2(\boldsymbol{x})} e^{-i2\pi \gamma \Delta B_0(\boldsymbol{x}) t} d\boldsymbol{x}. \tag{2.8}$$

2.1.2 Spatial Encoding

MRI attempts to resolve the measured signal $\boldsymbol{s}(t)$ into contributions from each spatial location, however the signal described by Eq. (2.8) provides no means for doing this. Standard MRI methods encode the signal location by applying linear gradient fields of the form $\boldsymbol{B}(\boldsymbol{x}) = (\boldsymbol{G} \cdot \boldsymbol{x})\, \hat{\boldsymbol{z}}$. Neglecting ΔB_0 and T_2 for the simplicity, the measured signal in the presence of an applied gradient field is

$$s(t) \propto 2\pi f_0 \int_{V_{\text{sample}}} \rho(\boldsymbol{x}) e^{-i2\pi \gamma \int_0^t \boldsymbol{G}(\tau) d\tau \cdot \boldsymbol{x}} d\boldsymbol{x}. \tag{2.9}$$

Defining $\boldsymbol{k}$ as

$$\boldsymbol{k} = \gamma \int_0^t \boldsymbol{G}(\tau) d\tau, \tag{2.10}$$

the encoded signal can be written as

$$s(\boldsymbol{k}) = \int_{V_{\text{sample}}} \rho(\boldsymbol{x}) e^{-i2\pi \boldsymbol{k}\cdot\boldsymbol{x}} d\boldsymbol{x}, \tag{2.11}$$

and we see that the signal as a function of the spatial encoding variable $\boldsymbol{k}$ is related to $\rho(\boldsymbol{x})$ by the Fourier transform. Therefore $\rho(\boldsymbol{x})$ can be reconstructed from a discrete set of samples of $\{s(\boldsymbol{k}_m)\}_{m=1}^M$ via the application of an inverse Fourier transform.[1]

2.1.3 Field Inhomogeneity Estimation

In many applications it is important to be able to estimate $\Delta B_0(\boldsymbol{x})$. The basic principle behind most estimation schemes (referred to as *field mapping* schemes) is to acquire two data sets (s_1 and s_2) and to make the delay between the excitation and data acquisition differ between the data sets by a time τ. In practice, the time spent acquiring the signal from a single excitation is much smaller than T_2 or $1/\Delta f_0$, where $\Delta f_0 := \gamma \Delta B_0$. Therefore, denoting the time between the excitation pulse and the acquisition of s_1 as T_E (referred to as the echo time), the reconstructions from s_1 and s_2 can be written as

$$\rho_1(\boldsymbol{x}) = \rho(\boldsymbol{x}) e^{-T_E/T_2(\boldsymbol{x})} e^{-i2\pi \Delta f_0(\boldsymbol{x}) T_E} \tag{2.12}$$

and

$$\rho_2(\boldsymbol{x}) = \rho(\boldsymbol{x}) e^{-(T_E+\tau)/T_2(\boldsymbol{x})} e^{-i2\pi \Delta f_0(\boldsymbol{x})(T_E+\tau)}, \tag{2.13}$$

[1] In practice, most current MRI applications measure the signal using multiple receiver coils and by incorporation of the sensitivity profiles into the reconstruction scheme can reconstruct $\rho(\boldsymbol{x})$ free of sensitivity profile weighting.

respectively. Δf_0 can thus be computed from the phase difference $\Delta\phi$ between ρ_1 and ρ_2 according to

$$\Delta f_0(\boldsymbol{x}) = \frac{\Delta\phi(\boldsymbol{x})}{2\pi\tau}. \tag{2.14}$$

2.2 Magnetic Resonance Spectroscopic Imaging

2.2.1 Chemical Shift

Like MRI, MRSI is concerned with the localization of the NMR signal; the difference between the two methods is that MRSI attempts to localize the signal over space as well as spin population. For example, the goal of a typical MRSI experiment could be to determine the spatial concentration distributions of various molecules within a sample. In this case, the ^{1}H nuclei in the different molecules could be could be considered different spin populations. These populations could also be divided even further, for instance, the ^{1}H nuclei in different chemical groups within the same type of molecule are generally considered different spin populations.

In all practical samples, the resonant frequencies of spins in different chemical environments will be shifted from f_0. This frequency shift δf is known as the *chemical shift* and can be modeled as

$$\delta f = -\gamma B_0 \sigma, \tag{2.15}$$

where σ is called the *shielding constant*, and can take on positive or negative values, typically on the order of 10^{-6}. The chemical shift results from the interaction between the nuclear spin and surrounding electrons. As illustrated in Fig. 2.1, electron current density distributions perturb the magnetic field "seen" by the nuclear spin, effectively "shielding" it from the applied B_0 field and thereby causing a shift in the resonant frequency. The amount of shielding is proportional to the applied $\boldsymbol{B}_0$ field as described by Eq. (2.15) [19].

Mathematically, the dependence of the measured signal on δf can be mod-

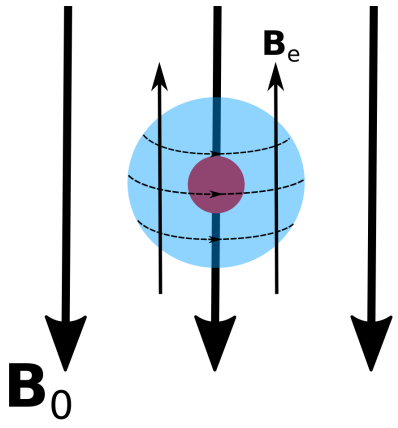

Figure 2.1: Illustration of the chemical shielding effect. In diamagnetic materials, the presence of the applied field $\boldsymbol{B}_0$ induces currents in ground-state electron distributions (blue) resulting in the creation of an opposing magnetic field $\boldsymbol{B}_e$ which "shields" the nucleus (red) and results in a shift in its resonant frequency.

eled through the introduction of a frequency dependence in Eq. (2.8), i.e.,

$$s(t) = \int_{V_{\text{sample}}} \int_{-\infty}^{\infty} \rho(\boldsymbol{x}, f) e^{-t/T_2(\boldsymbol{x},f)} e^{i2\pi f t} e^{-i2\pi\gamma\Delta B_0(\boldsymbol{x})t} df\, d\boldsymbol{x}. \tag{2.16}$$

The goal of MRSI is to resolve the contributions to $s(t)$ spatially and spectrally. This is achieved by performing spectral encoding during the data acquisition period in addition to spatial encoding provided by gradient fields. After performing the integration over frequency, the spatially and spectrally encoded signal can be written as

$$s(\boldsymbol{k}, t) = \int_{V_{\text{sample}}} \rho(\boldsymbol{x}, t) e^{-i2\pi\boldsymbol{k}\cdot\boldsymbol{x}} e^{-i2\pi t\Delta f_0(\boldsymbol{x})} d\boldsymbol{x}, \tag{2.17}$$

where $\rho(\boldsymbol{x}, t)$ is the defined as

$$\rho(\boldsymbol{x}, t) = \int_{-\infty}^{\infty} \rho(\boldsymbol{x}, f) e^{-t/T_2(\boldsymbol{x},f)} e^{i2\pi f t} df. \tag{2.18}$$

With this formulation MRSI attempts to reconstruct $\bar{\rho}(\boldsymbol{x}, f)$, the Fourier counter part of $\rho(\boldsymbol{x}, t)$. This is typically referred to to as the spatiospectral spin density distribution.

2.2.2 Major Challenges

The major challenges in MRSI are a result of the inherent insensitivity of the NMR phenomenon. The reason for this insensitivity is that signal strength is proportional to the equilibrium spin state population difference ($\Delta N_{\pm}$) which is very small, typically on the order of parts-per-million (ppm). For example, consider a spin population at room temperature (293 K) placed in a field of 3 T (the field strength of many modern MRI scanners). According to Eq. (2.2), in a population of a million spins, $\Delta N_{\pm}$ would only be about 35. The reason that MRSI is possible is that the number of spins in a sample tends to be very large. Consider the chemical N-acetylaspartate (NAA), a brain metabolite often observed in *in vivo* ^{1}H MRSI of the human brain. The methyl group of NAA gives rise to a prominently observed spectral peak in $\rho(\boldsymbol{x}, f)$, and the typical *in vivo* concentration of NAA is roughly 10 mmol/L [20]. Therefore, in a typical 1 mm^3 volume at body temperature (310 K) there are approximately 20×10^{15} nuclear spins associated with the spectral peak and the $\Delta N_{\pm}$ is approximately 70×10^{10}.

The result of this insensitivity is to create a very poor trade off between acquisition speed, SNR, and resolution. For a given acquisition time, higher resolution results in lower SNR. Successive measurements can be averaged together to increase the SNR; however, this requires increased scan time. Moreover, the trade-off is sub-linear. SNR increases proportionally to the square-root of the number of averages while the imaging time is directly proportional to the number of averages.

An additional challenge faced by *in vivo* ^{1}H MRSI, is the presence of signals from water and lipids. The concentrations of water and lipids are three to four orders of magnitude larger than those of the chemicals of interest (e.g. brain metabolites and neurotransmitters) as shown if Fig. 2.2. Separating these "nuisance" signals from the signals of interest is a considerable challenge, and considerable effort has been done to address this problem [16, 21–26].

2.2.3 Chemical Shift Imaging

The most common acquisition scheme for MRSI is chemical shift imaging (CSI). Proposed by Brown, et. al. in the early 1980s [5], CSI performs spatial encoding using pulsed gradient waveforms between excitation and

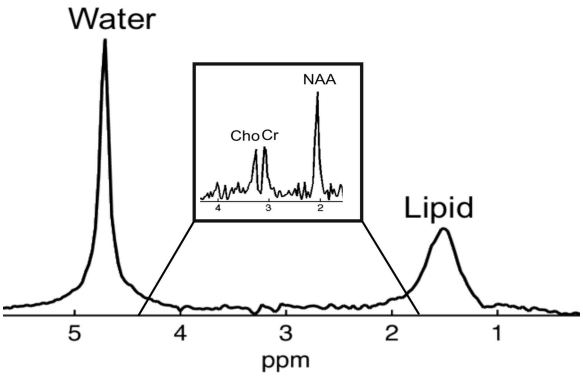

Figure 2.2: An *in vivo* ^{1}H MRSI voxel spectrum showing the overshadowing effect the nuisance signals have on brain metabolites such as N-acetylaspartate (NAA), creatine (Cr), choline (Cho). The cut-out shows a blown up portion of the spectrum after the water and lipid signals have been removed and reveals the presence of the metabolite signals.

data acquisition (or readout). This type of spatial encoding is called phase encoding. Figure 2.3 shows several different types of two-dimensional (2D) CSI pulse sequences, and Fig. 2.4 illustrates the sampling trajectory in ($\boldsymbol{k}$,t)-space. Spectral encoding is achieved solely through temporal sampling of the FID signal, and the timing of the gradient pulses is kept the same for each excitation to ensure that the same spectral encodings are acquired for each spatial encoding.

By acquiring spatial encodings $\{\boldsymbol{k}_m\}_{m=1}^M$ and spectral encodings $\{t_n\}_{n=1}^N$ that satisfy the Nyquist requirements of the imaging object $\rho(\boldsymbol{x}, f)$, accurate reconstructions $\hat{\tilde{\rho}}(\boldsymbol{x}, f)$ can be computed from the data samples $\boldsymbol{s}(\boldsymbol{k}_m, t_n)$ using the discrete Fourier transform (DFT)

$$\hat{\tilde{\rho}}(\boldsymbol{x}, f) = \sum_{n=1}^{N} \sum_{m=1}^{M} s\left(\boldsymbol{k}_m, t_n\right) e^{i2\pi(\boldsymbol{k}_m \cdot \boldsymbol{x} + t_n f)}. \tag{2.19}$$

Because only one spatial encoding is acquired for each excitation, acquiring the needed number of spatial encodings for high resolution reconstructions is very time consuming. In practice CSI can only be used to acquire data with limited $\boldsymbol{k}$-space coverage, and DFT reconstructions of CSI data often suffer from Gibbs ringing artifacts. In order to achieve reconstructions with both high spectral and spatial resolution, more advance data acquisition and image reconstruction schemes are needed.

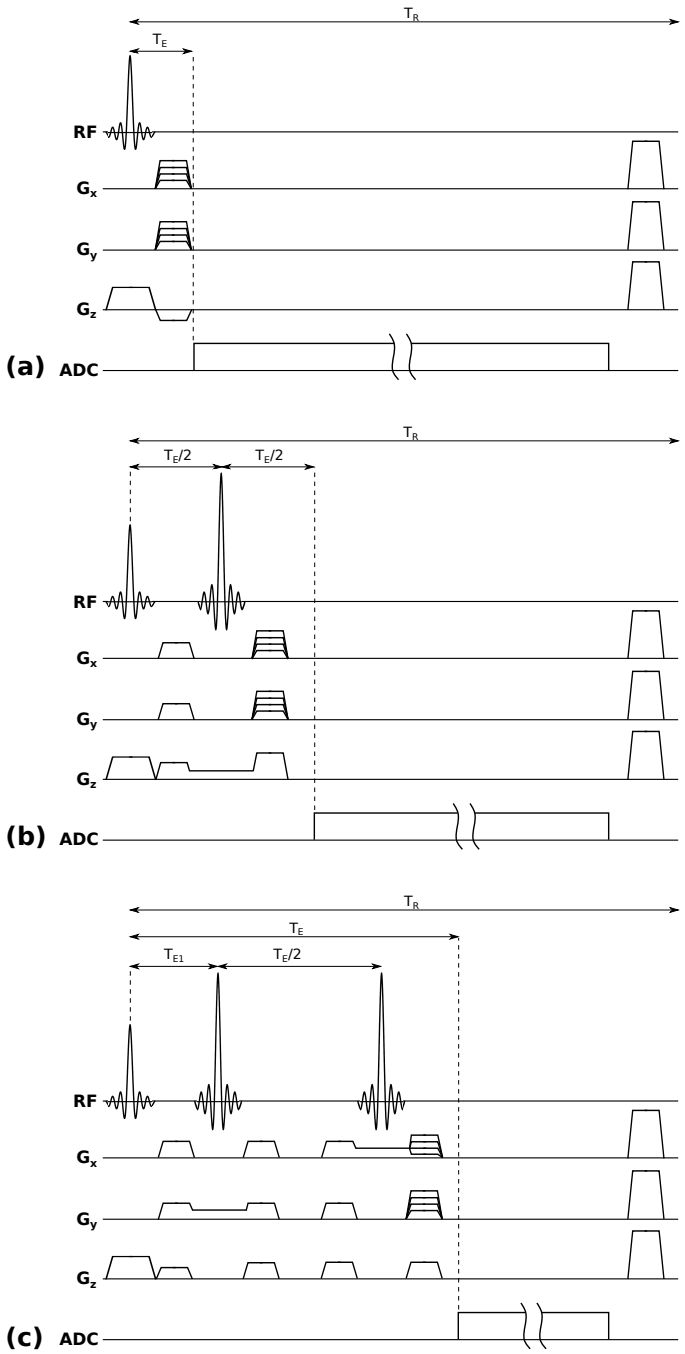

Figure 2.3: Several different CSI pulse sequences. (a) An FID CSI sequence. (b) A spin echo (SE) CSI sequence. (c) A point resolved spectroscopy (PRESS) sequence. Unlike the sequences in (a) and (b), which excite a z-slice volume of the sample, the PRESS sequence can select a localized cubic volume of the sample and therefore offers better signal localization.

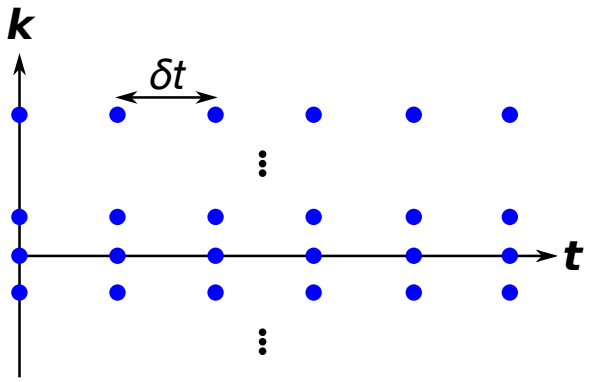

Figure 2.4: Sampling trajectory of a CSI sequence. In each repetition a line of samples (blue) is acquired along time for a single k-space location (i.e., one row). The spectral bandwidth of CSI sequences is equal to the reciprocal of the readout dwell time, δt. Note, in this figure all of the spatial encoding dimensions have been collapsed onto the k-axis.

2.2.4 Echo-Planar Spectroscopic Imaging

Echo-planar based spectroscopic imaging (EPSI) is a popular type of scheme for accelerated MRSI. EPSI uses oscillating gradient waveforms to acquire multiple spatial and spectral encodings during the readout period of each excitation (Fig. 2.5). Spatial encoding is achieved by sampling in the presence of the applied gradient waveforms (known as frequency encoding), and the spectral encoding is determined by the time between oscillations which is called the echo-spacing. Additional spectral encoding bandwidth is often achieved by varying the time between excitation and the beginning of the oscillating wave forms; these time-shift based encodings are referred to as echo-shifts.

While many types of (k, t)-space trajectories are possible, one of the most popular is Cartesian EPSI, proposed by Posse in the mid 1990s [27]. In this method only one spatial dimension is encoded using frequency encoding. Because both spatial and spectral encoding is performed in each excitation, the needed number of excitations is dramatically less than CSI. For example, consider a 2D experiment where the time between repeated excitations (known as the repetition time or T_R) is 2 seconds and the number of needed spatial encodings along the x and y dimensions (M_x and M_y respectively) are both 32. The CSI experiment will require $M_x M_y$ excitations or approximately 34 minutes to acquire all of the needed encodings while the EPSI experiment will require only M_y excitations or approximately 1 minute.

The drawback of EPSI is that the required readout bandwidth is greatly increased. This leads to an increase in measurement noise (proportional to the square-root of the bandwidth [28, 29]) and therefore decreased SNR. Hence, in practice the acceleration in acquisition is reduced due to the need to acquire multiple averages. In addition to decreased SNR, the increased duty cycle of the gradient waveforms can lead to field drift, which combined with non-idealities in the gradient waveforms can result in reconstruction artifacts if left unaccounted for.

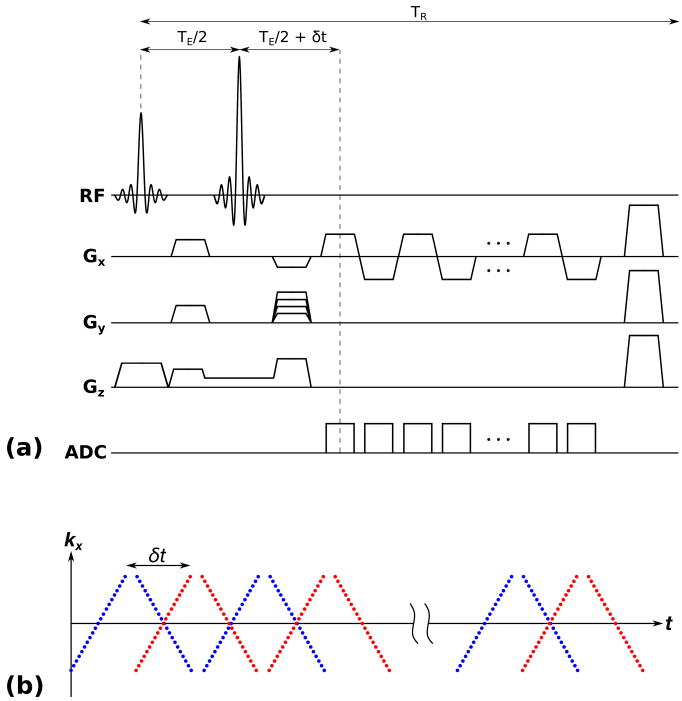

Figure 2.5: (a) A SE Cartesian EPSI sequence. Unlike a CSI sequence, oscillating gradient waveforms are played out during the FID period. The number of k_x encodings equals the number of samples acquired during the flat-top of each G_x oscillation and k_y encodings are achieved through pulsed G_y gradients (phase encoding) prior to the readout period. The time between oscillations and the number of different values of δt determine the spectral bandwidth. (b) Sampling trajectory of a Cartesian EPSI sequence for a single k_y encode and two echo-shifts. In each excitation period a zig-zag line of samples (blue and red dots) is acquired. The spectral bandwidth of the data is determined by the time between successive "V"s in the trajectory and the number of echo-shifts. In this figure the color of the samples is used to distinguish different echo-shifts.

CHAPTER 3

SUBSPACE-BASED MRSI

3.1 Signal Model

As described in Chapter 2, standard MRSI techniques provide a poor trade-off between speed, SNR, and resolution. While the development of more advanced acquisition schemes such as EPSI has helped to improved this trade-off [30–32], these schemes have yet to provide the improvements needed to make MRSI truly practical for a wide variety of scenarios. As such significant work has be done on the development of more advanced reconstruction schemes. In particular, through parsimonious modeling of the NMR signal, many reconstruction algorithms have been developed which are capable of providing accurate reconstructions from limited or sparsely-sampled data [14, 15, 33–41]. The common characteristic of this class of methods is a reduction in the degrees of freedom of the image function, $\bar{\rho}(\boldsymbol{x}, f)$, either through explicit or implicit constraints. This thesis is concerned with a class of subspace-based MRSI methods which use advanced acquisition and reconstruction techniques designed around a partially separable (PS) signal model.

3.1.1 Partial Separability

Subspace-based MRSI methods model the spatiospectral spin density distribution $\bar{\rho}(\boldsymbol{x}, f)$ as a partially separable function, i.e.,

$$\bar{\rho}(\boldsymbol{x}, f) = \sum_{l=1}^{L} u_l(\boldsymbol{x})\bar{v}_l(f), \tag{3.1}$$

or equivalently as

$$\rho(\boldsymbol{x}, t) = \sum_{l=1}^{L} u_l(\boldsymbol{x}) v_l(t), \tag{3.2}$$

where $\{v_l(t)\}_{l=1}^{L}$ (the Fourier counter parts of $\{\bar{v}_l(f)\}_{l=1}^{L}$) represent a set of square integrable temporal basis functions, $\{u_l(\boldsymbol{x})\}_{l=1}^{L}$ represent the corresponding spatial coefficients, and L is the model order (or separation rank) which is typically a small number [42–45]. The PS model was first proposed by Liang in [42] and offers several useful properties that make it particularly useful for accelerated imaging. First, as with other model-based reconstruction schemes, the PS model provides a reduction in degrees of freedom of the signal which enables accurate reconstruction from sparsely sampled data (this statement will be discussed more thoroughly in Section 3.1.2). Second, the separation of spatial and spectral subspaces of ρ increases the flexibility in the design of acquisition schemes. Third, and perhaps most importantly, the model is highly parsimonious; it can be shown that if L is made large enough, any square integrable $\rho(\boldsymbol{x}, t)$ can be approximated by Eq. (3.2) to any desired accuracy.

3.1.2 Mathematical Preliminaries of Subspace-Based Imaging

In this section we provide various definitions and theorems that will be utilized in this thesis. We present the definitions of a linear vector spaces, subspaces, norms, and inner products, and then illustrate how these are used in this thesis, concluding with a discussion of some mathematical properties of the PS model.

Much of the definitions in this section are very general and deal with definitions and operations on abstract algebraic sets. An important set operation is the *Cartesian product*.

Definition 1 *(Cartesian Product): The Cartesian product $\times$ is an operation on two sets $\mathcal{X}$ and $\mathcal{Y}$ that returns the set of ordered pairs of elements from each set, i.e., $\mathcal{X} \times \mathcal{Y} = \{(\boldsymbol{x}, \boldsymbol{y}) : \boldsymbol{x} \in \mathcal{X}, \boldsymbol{y} \in \mathcal{Y}\}$.*

Equipped with the definition of the Cartesian product we now provide the definitions of linear vector spaces and subspaces, the estimation of which is

the topic of this thesis.

Definition 2 *(Linear Vector Space (LVS)): A LVS is a set $\mathcal{X}$ and a scalar field* [1] *$\mathcal{F}$ equipped with an addition operation $+ : \mathcal{X} \times \mathcal{X} \to \mathcal{X}$ and a multiplication operation $\cdot : \mathcal{F} \times \mathcal{X} \to \mathcal{X}$. The addition operator must be commutative and associative, and the multiplication operator must be associative and distributive. $\mathcal{X}$ must also include the additive identity element $\mathbf{0}$, and $\mathcal{F}$ must include the multiplicative identity element $\mathbf{1}$.*

Definition 3 *(Subspace): Let $\mathcal{X}$ be a LVS and $\mathcal{S} \subset \mathcal{X}$. If $\mathcal{S}$ is also a LVS, then we say that $\mathcal{S}$ is a subspace.*

The next several definitions are important concepts needed for working with and describing LVSs.

Definition 4 *(Linear Combination): A vector $\boldsymbol{x}$ in a LVS $\mathcal{X}$ with scalar field $\mathcal{F}$ is a linear combination of the vectors $\{x_m\}_{m=1}^M \subset \mathcal{X}$ if there exist scalars $\{\alpha_m\}_{m=1}^M \subset \mathcal{F}$ such that $\boldsymbol{x} = \sum_{m=1}^M \alpha_m \boldsymbol{x}_m$.*

Definition 5 *(Span): The span of a set $\mathcal{S}$ in a LVS, denoted* $\operatorname{span}\{\mathcal{S}\}$*, is the set of all possible linear combinations of the vectors in $\mathcal{S}$.*

Definition 6 *(Linear Dependence): A vector $\boldsymbol{x}$ in an LVS $\mathcal{X}$ is linear dependent with respect to a set $\mathcal{S} \subset \mathcal{X}$ if $\boldsymbol{x}$ can be written as a linear combination of the vectors in $\mathcal{S}$. If $\boldsymbol{x}$ is not linearly dependent of $\mathcal{S}$,then $\boldsymbol{x}$ is said to be linearly independent of $\mathcal{S}$.*

Definition 7 *(Hamel Basis): A Hamel basis of an LVS $\mathcal{X}$ is any set of mutually linearly independent vectors $\mathcal{S}$ such that* $\operatorname{span}\{\mathcal{S}\} = \mathcal{X}$*. In this thesis, we will refer to a Hamel basis simply as a basis. The vectors in $\mathcal{S}$ are referred to as the basis vectors.*

An important result is that every LVS has a Hamel basis and that the number of vectors in every Hamel bases of an LVS is the same [46].

Definition 8 *(Dimension): The dimension of an LVS $\mathcal{X}$ is the number of vectors in any of its bases.*

[1] In general the field of an LVS can be any type of field, however this thesis will only be concerned with LVSs defined over scalar fields.

With the above definitions, it is now clear that $\rho(\boldsymbol{x}, t)$ is function which maps the Cartesian product of the spatial dimensions and the temporal dimension to a complex number, i.e., for a 2D image with spatial support $\mathcal{X} \subset \mathbb{R}^2$ and $t \in \mathcal{T} \subset \mathbb{R}_{\geq 0}$, $\rho(\boldsymbol{x}, t) : \mathcal{X} \times \mathcal{T} \to \mathbb{C}$. Furthermore, from Eq. (3.2) we see that for any $\boldsymbol{x}_m$, the temporal function $\rho(\boldsymbol{x}_m, t) \in \operatorname{span}\{v_l(t)\}_{l=1}$. From this observation it is clear that $\mathcal{V} := \operatorname{span}\{v_l(t)\}_{l=1} \subset \mathcal{T}$ is the L-dimensional temporal subspace of $\rho(\boldsymbol{x}, t)$. As will be discussed in Chapter 4, the goal of this thesis is the estimation of $\mathcal{V}$.

We now introduce the concept of a norm, which plays an important role in our understanding of the PS model as well as the formulation of the reconstruction methods proposed in this work.

Definition 9 *(Norm): A norm is a functional $\|\cdot\|$ defined on a vector space $\mathcal{X}$ that maps the space to $\mathbb{R}_{\geq 0}$ and satisfies the following properties: (i) $\|\boldsymbol{x}\| > 0$ unless $\boldsymbol{x} = \boldsymbol{0}$, (ii) for $\alpha \in \mathcal{F}$, $\|\alpha\boldsymbol{x}\| = |\alpha|\|\boldsymbol{x}\|$, (iii) for $\boldsymbol{x}, \boldsymbol{y} \in \mathcal{X}$, $\|\boldsymbol{x} + \boldsymbol{y}\| \leq \|\boldsymbol{x}\| + \|\boldsymbol{y}\|$.*

The most commonly known norm is the Euclidean norm, or ℓ_2 norm, defined on $\mathbb{C}^n$ and defined as

$$\|\boldsymbol{x}\|_2 := \left(\sum_{i=1}^{n} |x_i|^2\right)^{1/2}, \tag{3.3}$$

where x_i is the i^{th} element of $\boldsymbol{x}$. If instead of $\mathbb{R}^n$ we focus on the space of square integrable functions then we have the $\mathcal{L}_2$ norm

$$\|f(t)\|_2 := \left(\int |f(t)|^2 dt\right)^{1/2}. \tag{3.4}$$

Two other important norms utilized in this work are the Frobenius norm and the nuclear norm. These norms are defined for LVSs where each vector is a matrix, i.e., an element in $\mathbb{C}^{M \times N}$. The Frobenius norm, $\|\cdot\|_F$, is a straightforward generalization of the Euclidean norm, namely

$$\|\boldsymbol{X}\|_F = \left(\sum_{n=1}^{N}\sum_{m=1}^{M} |X_{m,n}|^2\right)^{1/2}, \tag{3.5}$$

where $X_{m,n}$ is the element of $\boldsymbol{X}$ in the m^{th} row and n^{th} column. The definition of the nuclear norm, $\|\cdot\|_*$ is less straightforward. Before defining it we first

must define the rank of a matrix and present a theorem.

Definition 10 *(Rank): The rank of a matrix is the number of linearly independent rows or columns that it contains.*

Theorem 1 *(SVD Theorem): Any rank L matrix $\boldsymbol{X} \in \mathbb{C}^{M\times N}$ can be decomposed as*

$$\boldsymbol{X} = \sum_{l=1}^{L} \sigma_l \boldsymbol{u}_l \boldsymbol{v}_l^H,$$

where $\{\sigma_l\}_{l=1}^L$ are all real with $\sigma_1 \geq \sigma_2 \geq \ldots \geq \sigma_L > 0$, and $\boldsymbol{u}_i^H \boldsymbol{u}_j = \boldsymbol{v}_i^H \boldsymbol{v}_j = \delta_{i,j}$. Here ^{H} denotes the complex-conjugate transpose operation $\overline{(\cdot)^T}$ and $\delta_{i,j}$ is the Kronecker delta. The values $\{\sigma_l\}_{l=1}^L$ are called the singular values of matrix $\boldsymbol{X}$, and the vectors $\{\boldsymbol{u}_l\}_{l=1}^L$ and $\{\boldsymbol{v}_l\}_{l=1}^L$ are called the left and right singular vectors respectively.

With the definition of the singular values of a matrix at hand we now give the definition of the nuclear norm, which is

$$\|\boldsymbol{X}\|_* := \sum_{l=1}^{L} \sigma_l, \tag{3.6}$$

where $\{\sigma_l\}_{l=1}^L$ are the singular values of $\boldsymbol{X}$.

An important property of norms is that they are convex.

Definition 11 *(Convexity): A mapping $f(\boldsymbol{x})$ from a LVS $\mathcal{X}$ onto $\mathcal{C}$ is said to be convex if $f\left(\lambda\boldsymbol{x} + (1-\lambda)\boldsymbol{y}\right) \leq \lambda f(\boldsymbol{x}) + (1-\lambda) f(\boldsymbol{y})$, $\forall \boldsymbol{x}, \boldsymbol{y} \in \mathcal{X}$. The mapping is said to be strictly convex if the previous inequality is strict for all $\boldsymbol{x} \neq \boldsymbol{y}$.*

Convexity plays an important role in the reconstruction methods proposed in Chapter 4, which involve the minimization of norms. An important fact about convex functions is that if a local minimizer of a convex function exists, then that minimizer achieves the global minimum of the function, furthermore if the function is strictly convex, then the global minimizer is unique. One of the major problems with computing minima is determining whether the computed minimum is a local minimum or global minimum; however, since the functionals that we seek to minimize are linear combinations of

convex functionals (which are easily shown to also be convex), we are freed of this problem.

In order to develop a quantitative metric for determining the error of a subspace estimate we make use of the concept of a projection.

Definition 12 *(Projection Operator): A projection operator is an idempotent linear transform mapping a LVS onto itself.*

Projections operators have very useful properties. To see why, we first introduce the definition of an inner product and a special type of LVS called a Hilbert space.

Definition 13 *(Inner Product): An inner product is a mapping from the Cartesian product of a LVS $\mathcal{X}$ with itself to its scalar field and which has several important properties. Denoting the inner product of $(\boldsymbol{x}, \boldsymbol{y}) \in \mathcal{X} \times \mathcal{X}$ as $\langle \boldsymbol{x}, \boldsymbol{y} \rangle$ these properties are: (i) $\langle \boldsymbol{x} + \boldsymbol{z}, \boldsymbol{y} \rangle = \langle \boldsymbol{x}, \boldsymbol{y} \rangle + \langle \boldsymbol{z}, \boldsymbol{y} \rangle$, (ii) $\langle \alpha \boldsymbol{x}, \boldsymbol{y} \rangle = \alpha \langle \boldsymbol{x}, \boldsymbol{y} \rangle$, (iii) $\langle \boldsymbol{x}, \boldsymbol{y} \rangle = \overline{\langle \boldsymbol{y}, \boldsymbol{x} \rangle}$, where the bar indicates the complex conjugate, (iv) $\langle \boldsymbol{x}, \boldsymbol{x} \rangle > 0$, $\forall \boldsymbol{x} \neq \boldsymbol{0}$.*

Two vectors are said to be *orthogonal* if their inner product is zero.

A normed LVS equipped with a inner product that is complete (contains the limits of all of its Cauchy sequences) is called a *Hilbert space*. When working with Hilbert spaces we have the following theorem which motivates the formulation of our subspace estimation error metric (described more in Chapter 5).

Theorem 2 *If $\mathcal{V}$ is a closed subspace in a Hilbert space $\mathcal{H}$, then the projection operator $\mathcal{P}\{\cdot\}$ with* $\text{range}\,\{\mathcal{P}\} = \mathcal{V}$ *is unique, and*

$$\mathcal{P}\{\boldsymbol{x}\} = \arg\min_{y \in \mathcal{V}} \|\boldsymbol{x} - \boldsymbol{y}\|,$$

where in this case $\|\cdot\|$ denotes the induced norm defined as

$$\|\boldsymbol{x}\| := \left(\langle \boldsymbol{x}, \boldsymbol{x} \rangle\right)^{1/2}.$$

We conclude this section with a more thorough discussion of the mathematical properties of the PS model. In the beginning of this chapter we claimed that the PS model was parsimonious. This claim was based on the following theorem [42].

Theorem 3 *Let $\mathcal{X}_1$ and $\mathcal{X}_2$ be two measure spaces. Let $\mathcal{H}$ be the set of square integrable functions defined on $\mathcal{X}_1 \times \mathcal{X}_2$, i.e., $\mathcal{H} = \mathcal{L}^2(\mathcal{X}_1 \times \mathcal{X}_2)$, then the set of all the functions in the form of $\sum_{l=1} \boldsymbol{u}_l(\boldsymbol{x}_1)\boldsymbol{v}_l(\boldsymbol{x}_2)$ $\forall$ $\boldsymbol{u}_l(\boldsymbol{x}_1) \in \mathcal{L}^2(\mathcal{X}_1)$ and $\boldsymbol{v}_l(\boldsymbol{x}_2) \in \mathcal{L}^2(\mathcal{X}_2)$ is dense in $\mathcal{H}$. Thus, for any $f(\boldsymbol{x}_1, \boldsymbol{x}_2) \in \mathcal{H}$, and appropriately defined $\boldsymbol{u}_l(\cdot)$ and $\boldsymbol{v}_l(\cdot)$*

$$\left\| f(\boldsymbol{x}_1, \boldsymbol{x}_2) - \lim_{L\to\infty} \sum_{l=1}^{L} \boldsymbol{u}_l(\boldsymbol{x}_1)\boldsymbol{v}_l(\boldsymbol{x}_2) \right\|_2 = 0.$$

This theorem shows that if we restrict $\rho(\boldsymbol{x}, t)$ to be a square integrable function[2] then by allowing L to be arbitrarily large, we can use the PS model to approximate $\rho(\boldsymbol{x}, t)$ to any desired precision.

Another important property of the PS model is that the measured signal is low rank. More specifically it can be shown that the *Casorati matrix* formed from arranging samples $\{(\boldsymbol{x}_m, t_n)\}_{m,n=1}^{M,N}$ into a matrix

$$\boldsymbol{C}(\rho) = \begin{pmatrix} \rho(\boldsymbol{k}_1, t_1) & \rho(\boldsymbol{k}_1, t_2) & \cdots & \rho(\boldsymbol{k}_1, t_N) \\ \rho(\boldsymbol{k}_2, t_1) & \rho(\boldsymbol{k}_2, t_2) & \cdots & \rho(\boldsymbol{k}_2, t_N) \\ \vdots & \vdots & \ddots & \vdots \\ \rho(\boldsymbol{k}_M, t_1) & \rho(\boldsymbol{k}_M, t_2) & \cdots & \rho(\boldsymbol{k}_M, t_N) \end{pmatrix} \tag{3.7}$$

will have a rank of at most L [42]. This is an incredibly useful property since it implies that the true measured image has at most $L(M + N)$ degrees of freedom and can therefore be reconstructed from sparsely sampled data.

3.2 Applications of Subspace Imaging in MRSI

We now briefly discuss two applications of subspace-based imaging in MRSI, namely the recently introduced SPICE framework for accelerated, high-resolution MRSI [14, 15, 17] and the union-of-subspaces method for ^{1}H MRSI [16]. The underlying theme in these methods is that they utilize the separation of the spatial and temporal subspaces provided by the PS model and perform reconstructions using a two-step procedure with explicit subspace constraints.

[2]This is a reasonable assumption in MRSI since $\rho(\boldsymbol{x}, t)$ represents the signal from a physical object. More specifically, according to the development in Chapter 2, $\rho(\boldsymbol{x}, t)$ will be square-integrable since it will have finite spatial support, and be exponentially bounded in time (as a result of T_2 decay).

3.2.1 The SPICE Imaging Framework

Spectroscopic imaging by exploiting spatiospectral correlation (SPICE) is a method (or more accurately, a framework) for performing accelerated MRSI. The acceleration provided by the method comes from a careful combination of accelerated acquisition schemes like EPSI with advanced reconstruction algorithms.

The low rank property of the PS model means that accurate reconstructions of $\rho(\boldsymbol{x}, t)$ may be estimated from sparsely sampled or noisy data, thereby allowing for significant reductions in acquisition time. Due to the inherently low SNR of MRSI data, however, care must be taken as to how the data is sampled and reconstructed. For instance, given a fully sampled but noisy data set $\{s(\boldsymbol{k}_m, t_n)\}_{m,n=1}^{M,N}$, and assuming the model order L is known, a denoised reconstruction could be obtained from the following procedure:

1. Arrange the data into a Casorati matrix $\boldsymbol{C}_s$ as

$$\boldsymbol{C}(s) = \begin{pmatrix} s(\boldsymbol{k}_1, t_1) & s(\boldsymbol{k}_1, t_2) & \cdots & s(\boldsymbol{k}_1, t_N) \\ s(\boldsymbol{k}_2, t_1) & s(\boldsymbol{k}_2, t_2) & \cdots & s(\boldsymbol{k}_2, t_N) \\ \vdots & \vdots & \ddots & \vdots \\ s(\boldsymbol{k}_M, t_1) & s(\boldsymbol{k}_M, t_2) & \cdots & s(\boldsymbol{k}_M, t_N) \end{pmatrix}, \tag{3.8}$$

   and compute the denoised Casorati matrix as the solution to

$$\hat{\boldsymbol{C}} = \arg \min_{\text{rank}\{\boldsymbol{C}\}=L} \|\boldsymbol{C}(s) - \boldsymbol{C}\|_F. \tag{3.9}$$

   $\hat{\boldsymbol{C}}$ is referred to as the *rank-L truncation* of $\boldsymbol{C}(s)$ and can be computed using the SVD of $\boldsymbol{C}(s)$ as

$$\hat{\boldsymbol{C}} = \sum_{l=1}^{L} \sigma_l \boldsymbol{u}_l \boldsymbol{v}_l^H, \tag{3.10}$$

   where σ_l, $\boldsymbol{u}_l$, and $\boldsymbol{v}_l$ refer to the l^{th} singular values and vectors of $\boldsymbol{C}(s)$ [44].

2. Use the inverse DFT to compute $\rho(\boldsymbol{x}, t)$ from the values of $\hat{\boldsymbol{C}}$.

While computationally tractable and simple, this method yields inaccurate results in the presence of very strong noise [15]. Moreover, it provides no

means of handling sparsely sampled or under-sampled data, and thus cannot provide the level of acceleration desired.

The SPICE framework utilizes an explicit subspace approach enabled by the separation of the spatial and temporal subspaces provided by the PS model. This separation enables SPICE to accurately reconstruction $\rho(\boldsymbol{x}, t)$ from data acquired in the form of two data sets,[3] one with limited k-space coverage (low resolution) but dense temporal sampling and one with extended k-space coverage but sparse temporal sampling (see Fig. 3.1). These two data sets will hereafter be referred to as $\mathcal{D}_1$ and $\mathcal{D}_2$ respectively. The reconstruction is then performed in two steps:

1. Temporal basis vectors $\{v_l(t)\}_{l=1}^{L}$ for the temporal subspace $\mathcal{V}$ are estimated using the samples from $\mathcal{D}_1$.

2. The spatial coefficients $\{u_l(\boldsymbol{x})\}_{l=1}^{L}$ are estimated as the solution to the following optimization problem (referred to as a regularized least-squares problem).

$$\hat{\boldsymbol{U}} = \arg\min_{\boldsymbol{U}} \|\boldsymbol{s}_2 - \mathcal{F}_2\{\boldsymbol{U}\hat{\boldsymbol{V}}\}\|_2^2 + \lambda R(\boldsymbol{U}, \hat{\boldsymbol{V}}), \tag{3.11}$$

   where $\boldsymbol{s}_2$ is a vector of the samples from $\mathcal{D}_2$, $\mathcal{F}_2\{\cdot\}$ is the encoding operator for $\mathcal{D}_2$, $\hat{\boldsymbol{V}}$ is a matrix with rows made from the estimated basis vectors sampled onto the temporal grid of $\mathcal{D}_2$, $R(\cdot,\cdot)$ is a regularization functional designed to incorporate prior information into the reconstruction, and λ is a positive real number controlling the data consistency of the reconstruction, $\|\boldsymbol{s}_2 - \mathcal{F}_2\{\hat{\boldsymbol{U}}\hat{\boldsymbol{V}}\}\|_2$. The reconstruction of $\rho(\boldsymbol{x}, t)$ is then computed from a rearrangement of the elements of $\hat{\boldsymbol{U}}\hat{\boldsymbol{V}}$. $\bar{\rho}(\boldsymbol{x}, f)$ is easily obtained through a Fourier transform over t.

This two-step method has important advantages. For one, it is considerably more computationally tractable than a joint estimation of $\hat{\boldsymbol{U}}$ and $\hat{\boldsymbol{V}}$ and can easily handle sparsely sampled data through a modification of $\mathcal{F}_2$. More importantly, however, the validity of the PS model ensures the accuracy of $\hat{\boldsymbol{U}}$ and $\hat{\boldsymbol{V}}$ given the acquisition strategies for $\mathcal{D}_1$ and $\mathcal{D}_2$. While $\mathcal{D}_1$ does not contain enough spatial encodings to yield accurate high-resolution reconstructions, it does contain enough spectral encodings to yield an accurate

[3] In practice, these data sets do not necessarily need to be acquired separately.

estimation of $\hat{\boldsymbol{V}}$. The reverse is true for $\mathcal{D}_2$ which, while limited in its spectral encodings, will have enough spatial encodings to produce a high-resolution estimate of $\hat{\boldsymbol{U}}$. Furthermore, the incorporation of prior information into the estimations (such as knowledge of tissue boundaries provided by anatomical reference images) through R, combined with the reduction in the number of degrees of freedom provided by the explicit subspace constraint makes step 2 an over-determined problem. As such, the SNR of $\mathcal{D}_2$ can be very low and still provide accurate reconstructions, thereby enabling further acceleration.

In Chapter 5 we show results demonstrating the gains in speed and resolution provided by subspace-base imaging methods such as SPICE.

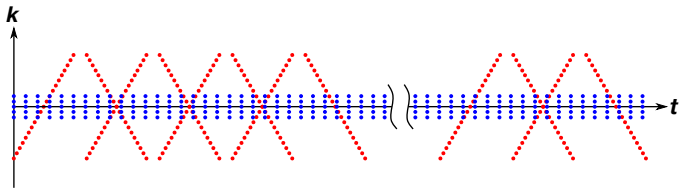

Figure 3.1: An example SPICE (k, t)-space sampling trajectory. Two sets of data are acquired, one with dense temporal sampling but limited k-space coverage (denoted by $\mathcal{D}_1$ and shown in blue), and one with sparse temporal sampling but extended k-space coverage (denoted by $\mathcal{D}_2$ and shown in red).

3.2.2 Union-of-Subspaces Based Nuisance Signal Removal

As discussed in Chapter 2, the presence of "nuisance" water and lipid signals in ^{1}H MRSI presents a significant challenge. The nuisance signals can be 1000 to 10000 times stronger than the chemical signals of interest, i.e., metabolites and neurotransmitters. As such the ability to separate or remove these nuisance signals from the data is of paramount importance to MRSI. Significant work has been done on this problem [21–26], and more recently a union-of-subspaces (UoS) method has been introduced for removing nuisance signals from data sets in the form $\mathcal{D}_1$ and $\mathcal{D}_2$ [16]. The method models $\rho(\boldsymbol{x}, t)$

as

$$\begin{aligned}\rho\left(\boldsymbol{x},t\right) =& W_M\left(\boldsymbol{x}\right)\sum_{p=1}^{P_M} u_{M,p}\left(\boldsymbol{x}\right) v_{M,p}\left(t\right) + \\ & W_W\left(\boldsymbol{x}\right)\sum_{p=1}^{P_W} u_{W,p}\left(\boldsymbol{x}\right) v_{W,p}\left(t\right) + \\ & W_L\left(\boldsymbol{x}\right)\sum_{p=1}^{P_L} u_{L,p}\left(\boldsymbol{x}\right) v_{L,p}\left(t\right),\end{aligned} \tag{3.12}$$

where $W_M(\boldsymbol{x})$, $W_W(\boldsymbol{x})$, $W_L(\boldsymbol{x})$ represent the spatial supports of the (metabolic) chemicals of interest, water signals, and lipid signals, and $\{u_{M,p}(\boldsymbol{x})\}_{p=1}^{P_M}$, $\{u_{W,p}(\boldsymbol{x})\}_{p=1}^{P_W}$, $\{u_{L,p}(\boldsymbol{x})\}_{p=1}^{P_L}$ and $\{v_{M,p}(t)\}_{p=1}^{P_M}$, $\{v_{W,p}(t)\}_{p=1}^{P_W}$, $\{v_{L,p}(t)\}_{p=1}^{P_L}$ represent the respective spatial coefficients and temporal basis functions for these signals. The removal is achieved by first estimating the water and lipid signals and then removing their contributions to the data.

The estimation of nuisance signals is performed in a similar fashion as prescribed in the SPICE framework:

1. Estimate the temporal basis vectors for each signal from $\mathcal{D}_1$.

2. Estimate the spatial coefficients through the solution of a regularized least-squares problem, namely

$$\hat{\boldsymbol{U}} = \arg\min_{\boldsymbol{U}} \|\boldsymbol{s}_2 - \mathcal{F}_2\{\mathbf{W}\boldsymbol{U}\hat{\boldsymbol{V}}\}\|_2^2 + \lambda R(\boldsymbol{U},\hat{\boldsymbol{V}}), \tag{3.13}$$

   where $\boldsymbol{U} = (\boldsymbol{U}_M, \boldsymbol{U}_W, \boldsymbol{U}_L)$, $\hat{\boldsymbol{V}} = \left(\hat{\boldsymbol{V}}_M^T, \hat{\boldsymbol{V}}_W^T, \hat{\boldsymbol{V}}_L^T\right)^T$, and $\mathbf{W}$ is the support operator $\mathbf{W} = \text{diag}\left\{\mathbf{W}_M, \mathbf{W}_W, \mathbf{W}_L\right\}$, with $\mathbf{W}_M$, $\mathbf{W}_W$, $\mathbf{W}_L$ corresponding to $W_M(\boldsymbol{x})$, $W_W(\boldsymbol{x})$, $W_L(\boldsymbol{x})$.

3. Compute the nuisance signal removed $\mathcal{D}_1$ and $\mathcal{D}_2$ data as $\hat{\boldsymbol{s}}_2 = \boldsymbol{s}_2 - \mathcal{F}_2\{\boldsymbol{C}_{ns}\}$ and $\hat{\boldsymbol{s}}_1 = \boldsymbol{s}_1 - \mathcal{F}_1\{\boldsymbol{C}_{ns}\}$, respectively; where $\boldsymbol{C}_{ns}$ is the nuisance signal contribution $\boldsymbol{C}_{ns} := \mathbf{W}_W\hat{\boldsymbol{U}}_W\hat{\boldsymbol{V}}_{\boldsymbol{W}} + \mathbf{W}_L\hat{\boldsymbol{U}}_L\hat{\boldsymbol{V}}_{\boldsymbol{L}}$, and $\mathcal{F}_1\{\cdot\}$ is the encoding operator for $\mathcal{D}_1$.[4]

The UoS model was shown to provide significantly improved nuisance signal removal compared with existing approaches [16].

[4]In practice, and an additional step to account for the discrepancy between the data from $\mathcal{D}_1$ and $\mathcal{D}_2$ is performed prior to the removal from s_1.

CHAPTER 4

SUBSPACE ESTIMATION

4.1 The Subspace Estimation Problem

One key problem in the applications of the subspace-based MRSI applications like the SPICE framework introduced in Chapter 3 is to accurately estimate the low-dimensional temporal (or spectral) subspace, i.e., $\mathcal{V} = \text{span}\,\{v_l(t)\}_{l=1}^{L}$ (or $\bar{\mathcal{V}} = \text{span}\,\{\bar{v}_l(t)\}_{l=1}^{L}$), from $\mathcal{D}_1$ corrupted by field inhomogeneity and noise. With the subspace determined, the image reconstruction problem reduces to a linear fitting problem with significantly fewer degrees-of-freedom, making high-resolution reconstruction with high SNR possible. However, this problem is challenging because typically only a limited number k-space encodings are available in $\mathcal{D}_1$ due to time and SNR constraints.

The aim of this thesis is to further addresses the problem of subspace estimation from limited data (within the SPICE framework). In particular, assuming the availability of a high-resolution B_0 field inhomogeneity map (easily obtained from accompanying anatomical scans) in addition to the MRSI data, we propose a regularized reconstruction formulation to remove the field inhomogeneity effects in $\mathcal{D}_1$. A singular value decomposition scheme is then applied to the field inhomogeneity corrected $\mathcal{D}_1$ to extract a set of temporal basis functions spanning the estimated subspace. In the following sections we describe our proposed method for estimating $\{v_l(t)\}_{l=1}^{L}$.

Based on the formulation of Eq. (2.17) in Chapter 2, we propose the following model for the measured (k,t)-space data $\{s(\boldsymbol{k}_m, t_n)\}_{m=1,n=1}^{M,N}$ obtained in an MRSI experiment,

$$\begin{aligned}\hat{s}\,(\boldsymbol{k}_m, t_n) &= s\,(\boldsymbol{k}_m, t_n) + \eta(\boldsymbol{k}, t) \\ &= \int \rho\,(\boldsymbol{x}, t_n)\, e^{-i2\pi \not{\gamma} \Delta B_0(\boldsymbol{x}) t_n} e^{-i2\pi \boldsymbol{k}_m \cdot \boldsymbol{x}} d\boldsymbol{x} + \eta(\boldsymbol{k}_m, t_n).\end{aligned} \tag{4.1}$$

Here η represents the noise in the measured data and is well modeled by complex white Gaussian noise. Combining this with the PS model in Eq. (3.2) used by SPICE, we can express $\hat{s}(\boldsymbol{k}_m, t_n)$ as

$$\hat{s}\left(\boldsymbol{k}_m, t_n\right) = \sum_{l=1}^{L} \int u_l(\boldsymbol{x}) v_l(t_n) e^{-i2\pi \gamma \Delta B_0(\boldsymbol{x}) t_n} e^{-i2\pi \boldsymbol{k}_m \cdot \boldsymbol{x}} d\boldsymbol{x} + \eta(\boldsymbol{k}_m, t_n). \quad (4.2)$$

As described in Chapter 3, the SPICE framework defines the imaging problem as recovering $v_l(t)$ (subspace estimation) from a data set with limited k-space coverage but dense temporal sampling ($\mathcal{D}_1$) and reconstructing $u_l(\boldsymbol{x})$ (spatial coefficient estimation) from a second data set with extended k-space coverage but sparse temporal sampling ($\mathcal{D}_2$) [14]. *In this thesis, we focus solely on the first problem.*

Considering that for most MRSI experiments, the dimension (L) of the subspace can be determined based on prior knowledge of the number of spectral components [44] and/or an empirical analysis of the given data, in the following discussion, we assume L is known (the issue of estimating L will be revisited at the end of this chapter and again in the subsequent chapter). Given L, in the ideal case of negligible field inhomogeneity ($\Delta B_0\left(\boldsymbol{x}\right) \approx 0$) and noise, Eq. (4.2) can be simplified into

$$s\left(\boldsymbol{k}_m, t_n\right) = \sum_{l=1}^{L} \bar{u}_l\left(\boldsymbol{k}_m\right) v_l\left(t_n\right), \quad (4.3)$$

where $\bar{u}_l\left(\boldsymbol{k}\right)$ is the Fourier transform of $u_l\left(\boldsymbol{x}\right)$. Thus, provided $M, N > L$, determination of a set of $\{v_l(t_n)\}_{l,n=1}^{L,N}$ can be easily done by computing the SVD of $\boldsymbol{C}\left(s\right)$, the Casorati matrix formed from the data in $\mathcal{D}_1$ (see Eq. (3.8)), selecting the L dominant right singular vectors, and taking their complex conjugate. This is due to the fact that $\boldsymbol{C}\left(s\right)$ has a rank upper-bounded by L (implied by Eq. (4.3)) and its row space is spanned by $\{\boldsymbol{v}_l\}_{l=1}^{L}$ where $\boldsymbol{v}_l := \left(v_l(t_1), v_l(t_2), \ldots, \boldsymbol{v}_l(t_N)\right)^T$ [42, 43].

However, ΔB_0 and η are usually not negligible in practice. In this case, as indicated by Eq. (4.2), ΔB_0 introduces significant spatiotemporal coupling, invalidating the PS model for the measured (k, t)-space signal unless a very high model order is used. Therefore, a key to accurately determining the underlying low-dimensional subspace lies in removing the effects of ΔB_0 on the given data, which is particularly challenging because of the limited k-space

coverage for $\mathcal{D}_1$. We propose to solve this problem using regularization-based field inhomogeneity corrected reconstruction which is described in Section 4.2.

4.2 Regularization-Based Field Inhomogeneity Corrected Reconstruction

First, we represent $\rho(\boldsymbol{x}, t_n)$ and $\Delta B_0(\boldsymbol{x})$ as follows:

$$\rho(\boldsymbol{x}, t_n) = \sum_{p=1}^{P} \rho\left(\boldsymbol{x}_p, t_n\right) \phi(\boldsymbol{x} - \boldsymbol{x}_p) \tag{4.4}$$

and

$$\Delta B_0(\boldsymbol{x}) = \sum_{p=1}^{P} \Delta B_0\left(\boldsymbol{x}_p\right) \psi(\boldsymbol{x} - \boldsymbol{x}_p), \tag{4.5}$$

where $\phi(\cdot)$ and $\psi(\cdot)$ are voxel basis functions with the former chosen as a delta function and the latter as a unit boxcar function, and $\{\boldsymbol{x}_1, \boldsymbol{x}_2, \ldots, \boldsymbol{x}_P\}$ represent the set of voxel locations at which $\Delta B_0(\boldsymbol{x})$ is given. These two choices of basis functions are widely used for image reconstruction because they yield accurate approximation with a large enough P. Moreover, they lead to the following simplified discretized imaging equation,

$$\hat{s}(\boldsymbol{k}_m, t_n) = \sum_{p=1}^{P} \rho\left(\boldsymbol{x}_p, t_n\right) e^{-i2\pi \gamma \Delta B_0(\boldsymbol{x}_p) t_n} e^{-i2\pi \boldsymbol{k}_m \cdot \boldsymbol{x}_p} + \boldsymbol{\eta}(\boldsymbol{k}_m, t_n), \tag{4.6}$$

which yields a matrix-vector multiplication form as

$$\hat{\boldsymbol{s}} = \mathbf{G}\mathbf{B}\boldsymbol{\rho} + \boldsymbol{\eta}, \tag{4.7}$$

where $\hat{\boldsymbol{s}}$ contains all the measured data $\hat{s}(\boldsymbol{k}_m, t_n)$, $\boldsymbol{\rho}$ contains all the voxel values $\rho\left(\boldsymbol{x}_p, t_n\right)$, $\boldsymbol{\eta}$ is the noise vector, $\mathbf{B}$ is a diagonal matrix containing the ΔB_0 phase terms from Eq. (4.6), and $\mathbf{G}$ is the Fourier encoding operator. When $\boldsymbol{k}_m$ all lie on a Cartesian grid (as in standard CSI acquisitions), $\mathbf{G}$ can be decomposed as $\mathbf{G} = \boldsymbol{\Omega}\mathbf{F}$, where $\boldsymbol{\Omega}$ is a grid sampling operator and $\mathbf{F}$ is the DFT operator.

Because of the limited k-space data available in $\mathcal{D}_1$ (i.e., $M \ll P$), Eq. (4.7) is a highly under-determined system. Thus, we propose to solve the problem by incorporating *a priori* information about $\boldsymbol{\rho}$ through a regularized reconstruction formulation:

$$\hat{\boldsymbol{\rho}} = \arg\min_{\boldsymbol{\rho}} \| \mathbf{GB}\boldsymbol{\rho} - \hat{\boldsymbol{s}} \|_2^2 + \lambda R(\boldsymbol{\rho}), \tag{4.8}$$

where $\| \cdot \|_2^2$ measures data consistency, $R(\cdot)$ represents the regularization functional, and λ is the regularization parameter.

4.2.1 Minimum Norm Least-Squares

It is useful to consider the case where no *a priori* information is used, i.e., $\lambda R(\cdot) = 0$. While not ideal, situations may arise in practice where no *a priori* information could be obtained about $\rho(\boldsymbol{x}, t)$; it could also be the case that a reconstruction free from the bias introduced by $R(\cdot)$ is desired. However, because the operator $\mathbf{G}$ will in general be surjective, a solution to Eq. (4.8) always exists but is not always unique. We therefore need a way to choose between multiple solutions.[1] One straightforward and popular choice is to select the solution which has the smallest ℓ_2 norm. This solution is known as the minimum norm, or minimum norm least-squares solution. Unfortunately, this method's performance can be sensitive the level of field inhomogeneity [47], especially with very limited k-space data.

4.2.2 Weighted ℓ_2 Regularization

Accordingly, one good choice of $R(\cdot)$ is the weighted ℓ_2 regularization functional [47], which enables incorporation of high-resolution information (missing in limited k-space data) obtained from auxiliary anatomical scans. More specifically, let

$$R(\boldsymbol{\rho}) = \sum_{p=1}^{P} \sum_{r=1}^{N_{dir}} w_{p,r} \left| \boldsymbol{d}_{p,r}^T \boldsymbol{\rho} \right|^2, \tag{4.9}$$

[1] The addition of the regularization term can be thought of as a way to make this choice based on *a priori* information. Good regularization terms make Eq. (4.8) a strictly convex problem by penalizing solutions with undesirable characteristics.

where $\boldsymbol{d}_{p,r}^T$ denotes the operator for computing the finite difference at the p^{th} voxel along the r^{th} direction and $w_{p,r}$ denotes a predetermined positive weight computed from the reference images. In particular, we compute the weights as described in [47,48], setting the values to be small where edges are expected and large elsewhere. When the weights are selected in this fashion the effect of $R(\boldsymbol{\rho})$ is to trade data consistency for the preferred high-resolution edge structure of the reference images.

4.2.3 Nuclear Norm Regularization

Another choice of $R(\cdot)$ is the following nuclear norm penalty denoted as

$$R(\boldsymbol{\rho}) = \|\boldsymbol{C}(\boldsymbol{\rho})\|_*, \tag{4.10}$$

where $\boldsymbol{C}(\cdot)$ denotes an operation that arranges $\boldsymbol{\rho}$ into a Casorati matrix. This choice is motivated by the fact that the PS model implies $\boldsymbol{C}(\boldsymbol{\rho})$ is low rank and also by the fact that the nuclear norm penalty has been shown to be an effective surrogate for encouraging low-rankness [49, 50].

4.3 Algorithm Considerations

The minimum norm solution is given by

$$\hat{\boldsymbol{\rho}} = (\mathbf{GB})^\dagger = \mathbf{B}^H\mathbf{G}^H\hat{\boldsymbol{s}}, \tag{4.11}$$

where † stands for the Moore-Penrose pseudo inverse. In practice, this solution is computed by multiplying the zero-filled DFT reconstruction of $\hat{\boldsymbol{s}}$ (i.e., $\mathbf{G}^H\hat{\boldsymbol{s}}$) by the conjugate of $e^{-i2\pi\not{\gamma}\Delta B_0(\boldsymbol{x}_p)t_n}$. Because of this, the minimum norm solution is sometimes referred to as the conjugate phase reconstruction [47].

Substituting Eq. (4.9) into Eq. (4.8) yields a least-squares problem with a unique solution given by

$$\hat{\boldsymbol{\rho}} = \left(\mathbf{B}^H\mathbf{G}^H\mathbf{GB} + \lambda\mathbf{D}^T\mathbf{WD}\right)^{-1}\mathbf{B}^H\mathbf{G}^H\hat{\boldsymbol{s}}, \tag{4.12}$$

where $\mathbf{D}$ denotes the row matrix of finite difference operators and $\mathbf{W}$ denotes

a diagonal matrix of the weights. We compute the solution using a linear conjugate gradient (CG) algorithm.

Integrating Eq. (4.10) into Eq. (4.8) and introducing an auxiliary variable $\boldsymbol{A} = \boldsymbol{C}(\boldsymbol{\rho})$, we reformulate the problem as

$$\begin{aligned} \hat{\boldsymbol{\rho}}, \hat{\boldsymbol{A}} = \quad & \arg\min_{\boldsymbol{\rho}, \boldsymbol{A}} \| \, \mathbf{GB}\boldsymbol{\rho} - \hat{\boldsymbol{s}} \, \|_2^2 + \lambda \|\boldsymbol{A}\|_* \\ s.t. \quad & \boldsymbol{A} = \boldsymbol{C}(\boldsymbol{\rho}). \end{aligned} \tag{4.13}$$

We then solve the problem in Eq. (4.13) using the alternating direction method of multipliers (ADMM) [51,52]. A detailed description of this efficient algorithm is given in Appendix A.2 along with a hybrid method combining both weighted ℓ_2 and nuclear norm regularization functionals for potential further improvement.

After obtaining $\hat{\boldsymbol{\rho}}$, we estimate the temporal subspace from the right singular vectors of $\boldsymbol{C}\left(\hat{\boldsymbol{\rho}}\right)$, although more sophisticated basis selection schemes can be used. It is worth noting that $\hat{\boldsymbol{\rho}}$ is not the final spatiotemporal/spatiospectral reconstruction for SPICE and does not have high spatial resolution due to the limited k-space coverage of $\mathcal{D}_1$. Nevertheless, with the effects of ΔB_0 effectively removed, it suffices for the purpose of subspace estimation.

4.3.1 Regularization Parameter Selection

One remaining practical issue is the selection of the regularization parameter. In this thesis we use different selection methods depending on whether or not the ground truth spatiospectral distributions are known. When the ground truth distributions are known, we introduce a subspace estimation error metric (described in Chapter 5) and select λ such that this error is minimized. When the ground truth distribution is not known (as in the case of experimentally obtained data) we use the well-known discrepancy principle [53] for λ selection in nuclear norm regularized reconstructions, and introduce a new method for λ selection in weighted ℓ_2 regularized reconstructions based on the idea of balancing the data consistency and regularization terms.

Because the weighted ℓ_2 reconstruction is linear and the distribution of $\boldsymbol{\eta}$ is known, we can estimate the values of these two terms for an ideal recon-

struction $\hat{\boldsymbol{\rho}}_0$. The expected value of the data consistency is

$$\mathbf{E}\{\| \boldsymbol{d} - \mathbf{GB}\hat{\boldsymbol{\rho}}_0 \|_2^2\} = \mathbf{E}\{\| \boldsymbol{\eta} \|_2^2\} \approx MN\sigma_\eta^2, \tag{4.14}$$

(where σ_η is the standard deviation of $\boldsymbol{\eta}$), and if we assume that the weights are chosen to be very small on edges of the the true image, $\boldsymbol{\rho}$, but not on smooth regions, then we will also have

$$\| \mathbf{WD}\boldsymbol{\rho} \|_2^2 \approx 0. \tag{4.15}$$

Hence, the major contribution to the penalty term will be the noise in the reconstruction $\boldsymbol{\xi}$. We can estimate λ as the value that equates the data consistency with the value of the regularization term, i.e.,

$$\lambda = \frac{MN\sigma_\eta^2}{\mathbf{E}\{\| \mathbf{WD}\boldsymbol{\xi} \|_2^2\}}. \tag{4.16}$$

If we approximate the distribution of $\boldsymbol{\xi}$ as the distribution of the noise in the minimum norm reconstruction $(\mathbf{GB})^\dagger\boldsymbol{\eta}$, and if σ_η^2 is known, it can be shown that

$$\mathbf{E}\{\| \mathbf{WD}\boldsymbol{\xi} \|_2^2\} = \sigma_\eta^2 \operatorname{Tr}\left\{((\mathbf{GB})^\dagger)^H \mathbf{D}^H \mathbf{W}^2 \mathbf{D} (\mathbf{GB})^\dagger\right\}. \tag{4.17}$$

In practice we estimate (4.17) by generating a random noise vector $\boldsymbol{\eta}$ and computing $\| \mathbf{WD}(\mathbf{GB})^\dagger\boldsymbol{\eta} \|_2^2$.

In Chapter 5 we provide simulation-based results comparing the subspace estimation errors of reconstructions made using the λ selected via this procedure to the minimum error values.

4.3.2 Model Order Determination

In practice, the model order L can often be determined based on prior knowledge of the spin system. For example in many types of samples the model order can be viewed as the number of chemicals in the sample or the number of different mixtures of chemicals in the sample, whichever is smaller. None the less, when the information about the spin system is less precise, as it often is for *in vivo* experiments, it is useful to have a quantitative procedure

to analyze a given data set and determine L. In this section we formulate a method for doing so.

Without ΔB_0, $\boldsymbol{C}(\hat{s})$ is equal to the sum of a rank-L matrix plus a random matrix. In this case, random matrix theory can be used to help determine L [54, 55]. In our case, removing the ΔB_0 effects will change the noise distribution which prevents the standard results of random matrix theory from being directly applicable. However, the effect of ΔB_0 correction on the distribution of the singular values of the random matrix can be determined empirically using a Monte-Carlo simulation. Then, the estimated singular value distribution of the (modified) noise matrix can be used to help adjust the value of L determined based on the available prior knowledge. More specifically, we can first estimate the expected values of the squared singular values of a Casorati matrix formed from ΔB_0 corrected i.i.d. Gaussian noise (with variance determined from the data), denoted as $\boldsymbol{E}[\xi_l^2]$ for the l^{th} singular value. Next, we write the SVD of $\boldsymbol{C}(\hat{\rho})$ in the following partitioned form:

$$\boldsymbol{C}(\hat{\rho}) = \begin{pmatrix} \boldsymbol{U}_1 & \boldsymbol{U}_2 \end{pmatrix} \begin{pmatrix} \boldsymbol{\Sigma}_1 & 0 \\ 0 & \boldsymbol{\Sigma}_2 \end{pmatrix} \begin{pmatrix} \boldsymbol{V}_1^H \\ \boldsymbol{V}_2^H \end{pmatrix}, \tag{4.18}$$

where $\boldsymbol{\Sigma}_1 = \text{diag}\{\sigma_1, \sigma_2, \ldots, \sigma_R\}$ and $\boldsymbol{\Sigma}_2 = \text{diag}\{\sigma_{R+1}, \sigma_{R+2}, \ldots, \sigma_{\min\{P,N\}}\}$, with $\sigma_1 \geq \sigma_2 \geq \cdots \geq \sigma_R \geq \cdots \sigma_{\min\{P,N\}}$. We then obtain a model order estimate $\hat{L}$ by selecting a value of R such that the set of $\{\sigma_l\}_{l=R+1}^{\min\{P,N\}}$ is most "similar" to $\{\boldsymbol{E}[\xi_l^2]\}_{l=1}^{\min\{P,N\}-R}$, i.e.,

$$\hat{L} = \arg \min_{R<R_{max}} \sum_{l=1}^{\min\{P,N\}-R} \left| \frac{\sigma_{l+R}^2}{\sum_{j=1}^{\min\{P,N\}-R} \sigma_{j+R}^2} - \frac{\boldsymbol{E}[\xi_l^2]}{\sum_{j=1}^{\min\{P,N\}-R} \boldsymbol{E}\left[\xi_j^2\right]} \right|, \tag{4.19}$$

where $R_{max} < \min\{P, N\} - 1$ is the largest rank allowed. To evaluate the performance of this estimator, we have performed further studies using simulated data which are presented in Chapter 5. Note that a similar method was used for determining spatially varying noise levels of MRI data in [56].

CHAPTER 5

METHODS AND RESULTS

We have evaluated the proposed method using both numerical simulations and experimental studies. The subspace estimation accuracy was evaluated quantitatively using simulated data (in the presence of a ground-truth) and qualitatively using experimental data (in the absence of a ground-truth). Furthermore, we demonstrate the method's practical utility by using it in a SPICE reconstruction of an *in vivo* data set.

5.1 Simulation Study

We used a high-resolution numerical MRSI phantom (illustrated in Fig. 5.1) similar to the one used in [14] for our study. The phantom contained brain metabolite spectra (N-acetylaspartate (NAA), creatine (Cr), choline (Cho), glutamate (Glu), glutamine (Gln), and myo-inositol (mI)) obtained from quantum mechanical simulations [57] of a spin echo sequence ($T_E = 30$ ms, bandwidth = 2 kHz) and incorporated realistic lineshape variation along with *in vivo* metabolite concentration ratios [20]. The generated ground-truth spatiotemporal distribution had a matrix size of $60 \times 60 \times 256$ (with the third dimension being the temporal axis). Rank truncation was then performed to generate a rank-16 ground-truth (i.e., $L = 16$) distribution. A reference image with a matrix size of 60×60 was also created for use with the weighted ℓ_2 correction method (Fig. 5.1b).

Data was generated from the rank-16 ground-truth distribution (according to Eq. (4.7)) with varying k-space sampling grid sizes (8×8, 12×12, 16×16, ..., 32×32) and corrupted by field inhomogeneity and noise of various levels. The field inhomogeneity was introduced through an experimentally acquired *in vivo* ΔB_0 map (Fig. 5.1a) which had been co-registered to the numerical

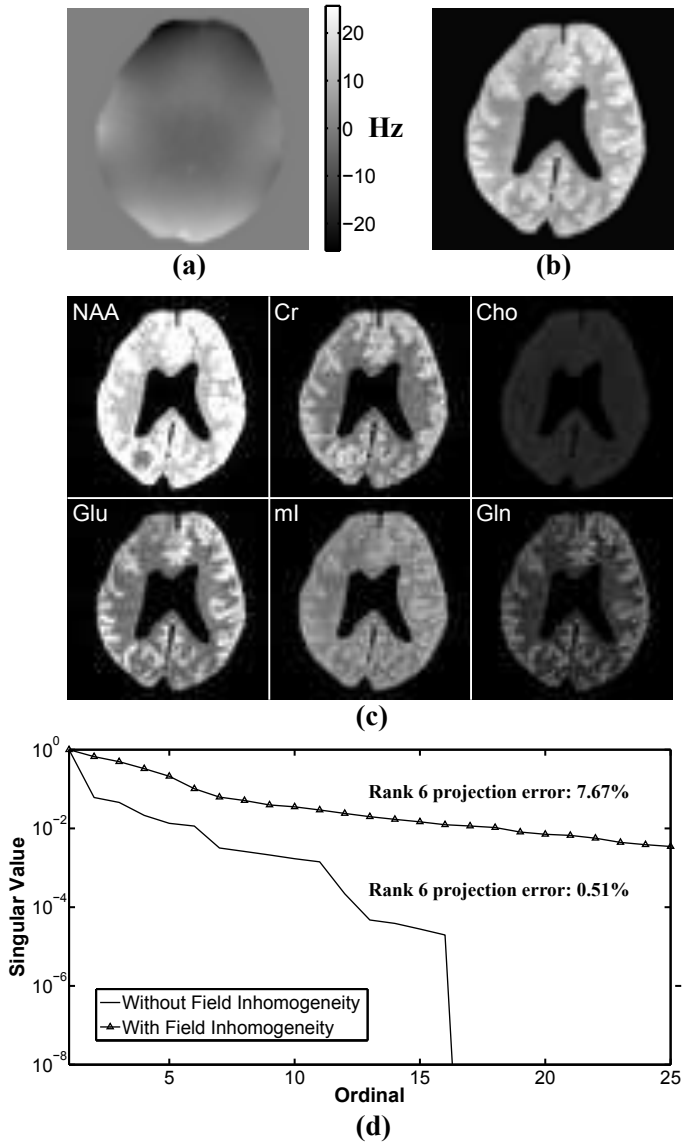

Figure 5.1: Numerical phantom: (a) ΔB_0 map and (b) anatomical image used in simulations. (c) Ground-truth metabolite distributions of the phantom, scaled according to their relative concentrations. The rank-increasing effect of ΔB_0 (see Section 4.1) is illustrated in (d) which shows the first 25 singular values of the numerical phantom with and without added ΔB_0. The rank 6 normalized subspace modeling errors with and without ΔB_0 are also provided for further to further illustrate this effect. Note that without ΔB_0 the rank is 16.

phantom. The SNR for the corrupted data was defined as

$$SNR = \frac{\|\bar{\boldsymbol{\rho}}\|_\infty}{\sigma_\eta}, \tag{5.1}$$

where σ_η is the spectral noise standard deviation, $\bar{\boldsymbol{\rho}}$ is the spatiospectral counterpart of $\boldsymbol{\rho}$, and $\|\cdot\|_\infty$ denotes the ℓ_∞ norm defined which is defined for a vector $\boldsymbol{x} = (x_1, x_2, \ldots, x_n)^T$ as

$$\|\boldsymbol{x}\|_\infty := \max_i |x_i| \,. \tag{5.2}$$

This SNR definition can be interpreted as the upper bound on metabolite peak SNR.

We performed field inhomogeneity correction using the simulated (k,t)-space data and used the corrected data to extract different sets of temporal bases. The accuracy of the resulting subspace estimates were quantitatively measured using the following normalized projection error:

$$e\left(\boldsymbol{C}, \boldsymbol{P}_e\right) = \frac{\|\boldsymbol{C} - \mathcal{P}_e\{\boldsymbol{C}\}\|_F}{\|\boldsymbol{C}\|_F}, \tag{5.3}$$

where $\boldsymbol{C}$ is the Casorati matrix formed from the fullysampled ground-truth data and $\boldsymbol{P}_e\{\cdot\}$ is the projection operator for the estimated temporal subspaces. The metric measures the normalized root-squared error between the true signal and its projection onto the estimated subspace. While other methods exist for comparing subspaces [58, 59], this "projection error" is more informative for our purpose since it reflects the ability of the estimated subspace to represent the underlying signal. Figure 5.1d shows the singular values and rank 6 projection errors of the ground-truth Casorati matrix with and without the applied ΔB_0, illustrating how the projection error is able quantify the subspace estimation error from the spatiospectral coupling effect of ΔB_0.

5.1.1 Comparison of Field Inhomogeneity Correction Algorithms

Figure 5.2a shows some representative results of subspace estimations from data of various k-space coverages using the three ΔB_0 correction methods

discussed (minimum norm, nuclear norm regularized, and weighted ℓ_2 norm regularized) as well as results from estimations made without ΔB_0 correction. In each case, the projection error in Eq. (5.3) was computed using the first 16 right singular vectors. Figure 5.2b shows the corresponding results for data corrupted with a higher level of noise and larger field inhomogeneity than for Fig. 5.2a (more specifically, half the SNR and twice the ΔB_0). As expected, the error generally decreases as k-space coverage increases, and furthermore, larger coverage is needed as ΔB_0 gets stronger and SNR gets lower.

The projection error curves for noise-only scenarios ($\Delta B_0(\boldsymbol{x}) = 0$) are also provided as "best-case" references. Comparison between the error curves of the ΔB_0 corrected reconstruction and the uncorrected reconstructions clearly show that there is a significant improvement in subspace estimation when field correction is utilized, and comparison with with the noise-only curves indicates that a 16×16 to 20×20 sampling grid provides sufficient k-space coverage for subspace estimation provided field correction is utilized.

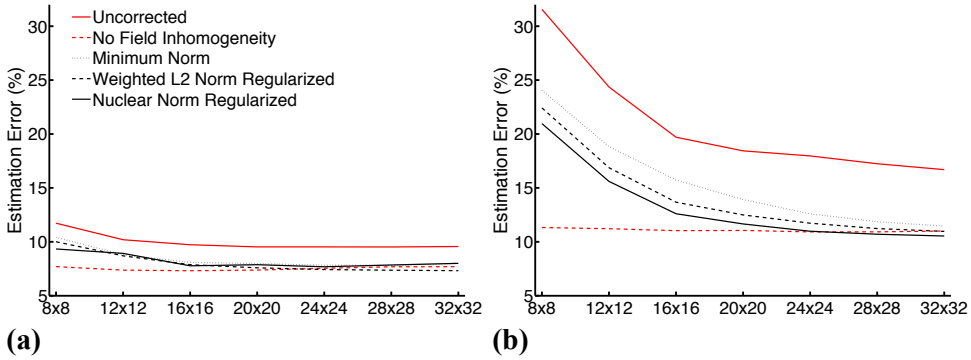

Figure 5.2: Subspace estimation errors defined in Eq. (5.3) calculated for the 16 (the true model order) dimensional subspaces estimated from uncorrected and ΔB_0 corrected data sets of various sizes simulated with (a) good/typical conditions (SNR 12, original ΔB_0) and (b) poor experimental conditions (SNR 6, $2\times$ original ΔB_0). The estimation errors present without field inhomogeneity are also provided for reference. The x-axis denotes data size (k-space coverage) for each data point on the curves.

The results also reveal that our nuclear norm regularized correction provides more robust estimation over a range of k-space grid sizes and ΔB_0 strengths. The ability of the nuclear norm correction scheme to provide better estimates than the minimum norm and weighted ℓ_2 schemes at smaller data sizes is particularly desirable for accelerated MRSI experiments. Additionally, Fig. 5.3 shows that regions where $\Delta B_0(\boldsymbol{x})$ varies rapidly, the nuclear

norm correction scheme is also capable of providing better correction of the more commonly known peak-broadening effect associated ΔB_0 [47, 60–62].

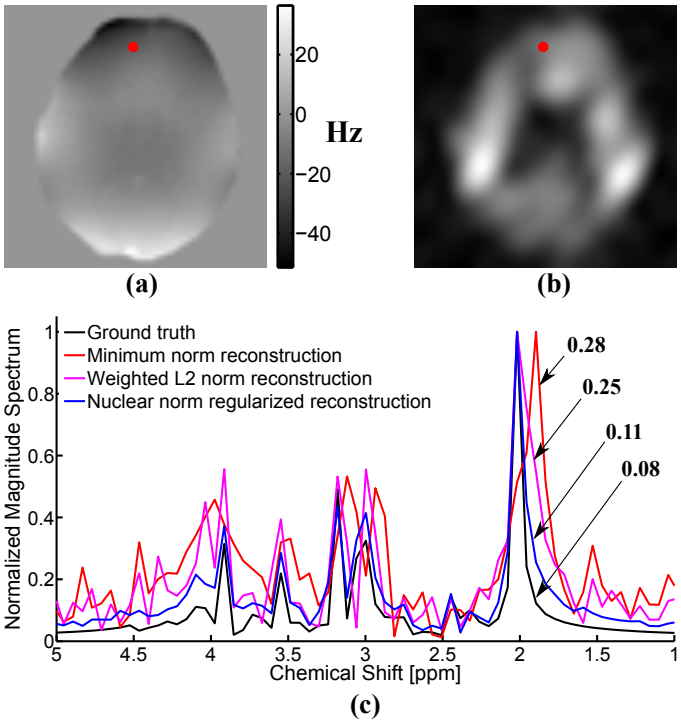

Figure 5.3: Illustration of the reduction in line shifting and broadening effects provided by the field corrected reconstructions. (a) ΔB_0 map and (b) minimum norm reconstruction energy distribution. (c) A spectrum from minimum norm (red), weighted ℓ_2 regularized (pink), and nuclear norm regularized (blue) reconstructions of simulated $\mathcal{D}_1$ data (8×8 encodings, 6 SNR, $2 \times \Delta B_0$) compared to the ground-truth spectrum (black). The widths in ppm of the NAA peaks are indicated with arrows. The location of the spectra is indicated by the red dot in (a) and (b).

In Figs. 5.2a-b and Fig. 5.3 a course-fine search over the values of λ was performed to minimize the projection errors for each scenario. Although this is not a viable selection strategy in practice (where the ground-truth is unknown), this optimization was done so that a more fair comparison between the field correction methods could be made. An added benefit of this procedure was that it provided estimates of the minimum projection errors which could then be used to test other λ selection schemes.

5.1.2 Validation of Weighted ℓ_2 Regularization Parameter Selection Method

We tested our proposed weighted ℓ_2 regularization parameter selection method (described in Section 4.3.1) by comparing the projection error curves obtained using the estimated values of λ to those obtained with the optimal values of λ. Figures 5.4a-b show the respective curves for the same scenarios as in Figs. 5.2a-b. The difference between projection errors obtained using the proposed λ selection method and the minimum error estimates are negligible, indicating that the proposed selection method is a viable strategy for subspace estimation from experimentally obtained data.

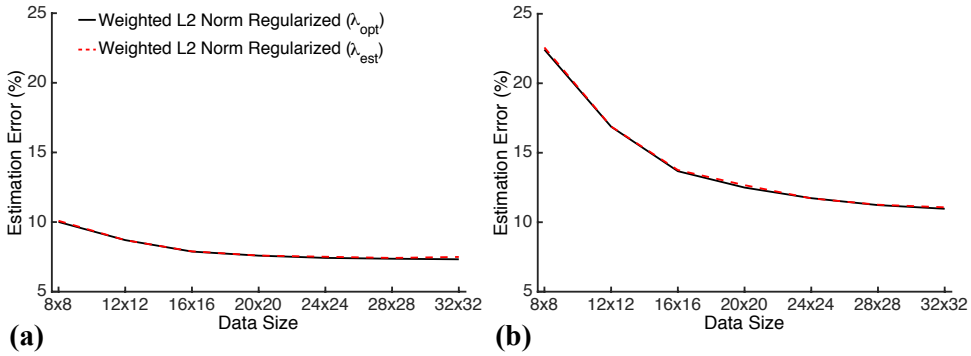

Figure 5.4: (a) and (b) are the same as in Fig. 5.2 except that here the error curves for the weighted ℓ_2 reconstructions using the optimal are compared with those made using the estimated (as described in the Section 4.3.1) regularization parameters. The x-axis denotes data size (k-space coverage) for each data point on the curves.

5.1.3 Validation of Model Order Estimator

In Monte-Carlo simulations using the numerical phantom data, we generated 50 independent realizations corrupted by noise and field inhomogeneity (the SNR was 12 and the ΔB_0 in Fig. 5.1a was used). We then computed the squared singular values of the Casorati matrices formed from the minimum norm ΔB_0 corrected data. The results of the simulation (Fig. 5.5a) show that the variation for squared singular values is very small, which indicates that the variance of our estimator should be small as well (a highly desirable characteristic of any estimator).

Figure 5.5a shows that using the proposed criterion in Eq. (4.19), we obtain a model order estimate of 4, which is reasonable given the limited number of spectral components in the phantom and the similarity of metabolite distribution patterns (Fig. 5.1c). The accuracy of this order estimate is further confirmed in Fig. 5.5b where it is shown that increasing the model order past 4 yields little change in estimation error regardless of the ΔB_0 correction method used.

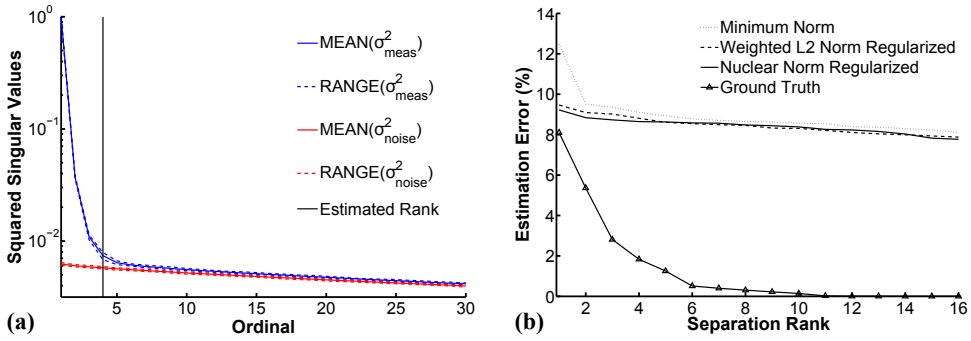

Figure 5.5: (a) Monte-Carlo results for our model order determination criteria from 16×16 simulated data corrected using the minimum norm reconstruction method. Only the first 30 squared singular values are shown. The dotted lines indicate the maximum and minimum squared singular values for the corresponding Casorati matrices over all realizations. The vertical black line identifies the estimated model order (i.e. $\hat{L} = 4$). (b) Normalized subspace estimation errors as defined in Eq. (5.3) calculated for subspaces of varying dimensionality estimated from 16×16 ΔB_0 corrected simulated data in Fig. 5.2a. The estimation error due solely to rank truncation of the ground truth data (dash-dotted line) is provided as a reference. Notice that increasing the model order past 4 results in little change in estimation error regardless of the field correction method used and that this behavior is consistent with the behavior of the error due solely to rank truncation.

5.2 Experimental Study

5.2.1 Phantom Experiment

Data was acquired from a customized brain metabolite phantom to further validate the simulation results. The phantom is a polymethylpentene cylindrical jar containing NaCl-doped water and ten vials with different diam-

eters (Fig. 5.6a). The vials were filled with metabolite solutions of physiologically relevant concentrations [20]. More specifically, the large vials (group 1 in Fig. 5.6) contained approximately 20 mmol/L NAA, 15 mmol/L Cr, 5 mmol/L choline-chloride (Cho) and 10 mmol/L mI; the medium vials (group 2) contained approximately 10 mmol/L NAA, 10 mmol/L Cr, 5 mmol/L Cho and 10 mmol/L mI; the small vials (group 3) contained approximately 15 mmol/L NAA, 10 mmol/L Cr, 5 mmol/L Cho and 10 mmol/L mI.

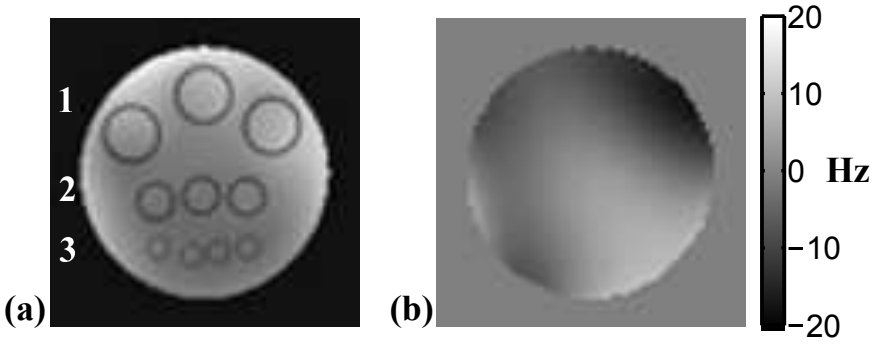

Figure 5.6: (a) Anatomical reference image and (b) estimated ΔB_0 map (in Hz) for the experimental phantom.

The experiment was conducted on a 3T Siemens Trio scanner (Siemens Healthcare USA) equipped with a 12-channel receiver head coil. A high-resolution CSI data set was obtained using a customized version of a commercial CSI sequence with the following parameters: $T_R/T_E = 1000/30$ ms, FOV $= 220\times220$ mm^2, excitation area $= 150\times150\times10$ mm^2, slice thickness $=$ 10 mm, k-space grid size $= 80\times80$ with elliptical sampling, FID length $= 512$, and spectral bandwidth $= 2000$ Hz. WET water-suppression [24] was also applied. The acquisition time was 1.3 hours. For reference, a gradient echo (GRE) image was obtained (grid size $= 192 \times 192$, $T_R/T_E = 50.0/3.58$ ms), and for ΔB_0 correction, a two-point Dixon method-based field map (grid size $= 128 \times 128$, $T_R/T_{E1}/T_{E2} = 600/9.84/12.3$ ms) was obtained immediately before and after the CSI sequence. The field maps were averaged together and then fitted to a fifth-order multivariate polynomial (Fig. 5.6).

After acquisition, the HSVD algorithm [63] was applied to the data from each coil in order to remove any residual water signal. The coil data was then combined using an SVD-based method [64]. A gold-standard spatial-spectral distribution was then computed from the 128×128 minimum norm reconstruction of the data followed by a spatial Hamming window and temporal

truncation to 256 time samples (for denoising).

$\mathcal{D}_1$ data of varying grid sizes were generated by retrospectively sampling the coil-combined CSI data. Temporal subspaces were estimated from the 128×128 DFT and nuclear norm regularized ΔB_0 corrected reconstructions. The gold-standard distribution was then projected onto the estimated subspaces for evaluation of the proposed method.

Figure 5.7 shows subspace estimation results based on the data from the experimental phantom and provides experimental verification of the importance of ΔB_0 correction for subspace estimation. Using the minimum norm reconstruction of the 80×80 CSI data as a gold-standard (Fig. 5.7a-b), the figure compares projections of the gold-standard onto subspaces estimated with nuclear norm regularized ΔB_0 correction (Fig. 5.7c-e) and without any correction (Fig. 5.7f-h). It is clear from the figure that the residual after projection is greatly reduced when ΔB_0 is utilized.

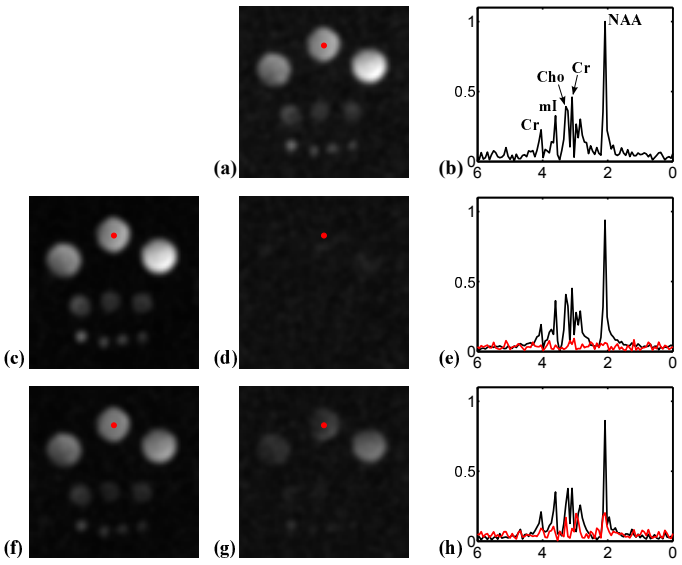

Figure 5.7: Effect of subspace estimation error on the spatiospectral distribution of the 80×80 CSI. (a) NAA peak integral from Hamming windowed and minimum norm ΔB_0 corrected reconstruction of the 80×80 CSI data. (b) Spectrum from the location indicated by the red dot in (a). (c) NAA peak integral after a projection of the spatiospectral distribution onto the subspace estimated from the nuclear norm regularized ΔB_0 corrected reconstruction of $\mathcal{D}_1$ data with 16×16 spatial encodings. (d) Peak integral of the residual. (e) Projected (black) and residual (red) spectra with respect to (b). (f-h) Corresponding results for a subspace estimated without ΔB_0 correction. The model orders of the estimated subspaces were 5. The x-axes denote chemical shift in ppm.

Figure 5.8 illustrates the effect of $\mathcal{D}_1$ k-space coverage on subspace estimation. Each row of the figure shows projections and residuals for $\mathcal{D}_1$ with k-space sampling grid sizes of 8×8, 16×16, and 32×32 respectively. As in simulation results, the residual error becomes very small for sampling grid sizes 16×16 or greater.

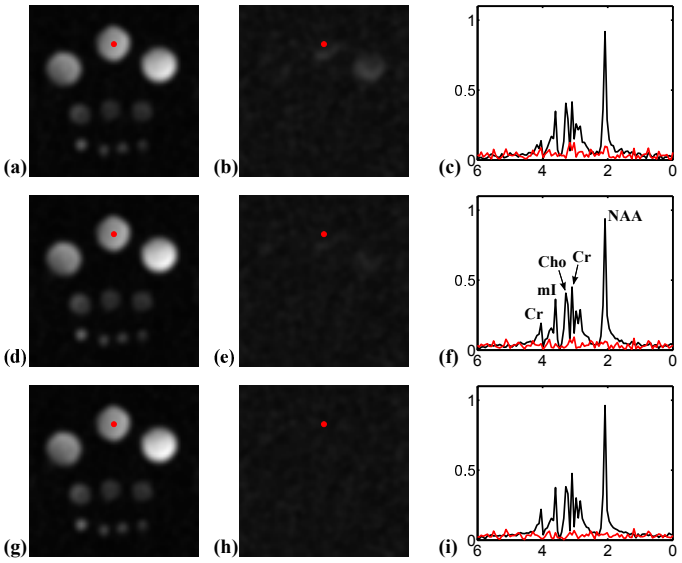

Figure 5.8: Effect of $\mathcal{D}_1$ k-space coverage. (a-c) are the same as Fig. 5.7c-e except that the $\mathcal{D}_1$ data had 8×8 encodings. (d-f) are the same as Fig. 5.7c-e. (g-i) show the results for $\mathcal{D}_1$ data with 32×32 encodings. The x-axes denote chemical shift in ppm.

Figure 5.9 illustrates the effect of model order selection. The figure shows results from the same nuclear norm regularized reconstruction as in Figs. 5.7c-e and Figs. 5.7d-f; however, the number of singular vectors used for the subspace varies with each row (1, 5, 9 respectively). While the residual is very large when only a one-dimensional subspace is used, it becomes very small after $L = 5$. This is the expected behavior since there are only three different solutions in the phantom. Moreover, these results indicate that the method is robust with respect to an overestimated model order.

5.2.2 *In Vivo* Experiment

In vivo ^{1}H MRSI data was acquired from a healthy volunteer (following approval from the local Institutional Review Board) using the same scanner and head coil described above. The same CSI sequence was used to obtain

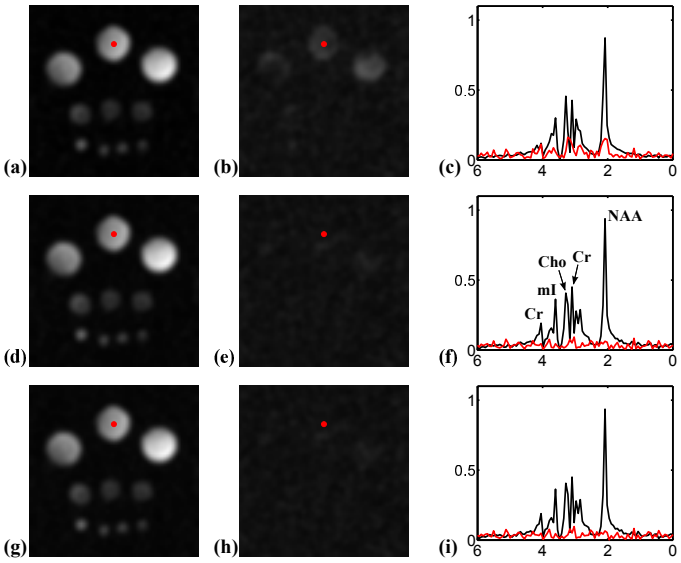

Figure 5.9: Sensitivity to model order selection. (a-c) are the same as Fig. 5.7c-e, except that a one-dimensional subspace was used. (d-f) are the same as Fig. 5.7c-e. (g-h) show the corresponding results with a nine-dimensional subspace estimate. The x-axes denote chemical shift in ppm.

low-resolution data with imaging parameters: $T_R/T_E = 1600/30$ ms, FOV = 220×220 mm^2, excitation area = 150×160 mm^2, slice thickness = 10 mm, grid size = 24×24, FID length = 512, and spectral bandwidth = 2000 Hz. WET pulses for water suppression and eight outer volume suppression bands [23] for lipid suppression were also used. The acquisition time was 15.4 minutes. High-resolution EPSI data was also obtained with: $T_R/T_E = 1600/30$ ms, grid size = 112×112, number of echoes = 60, readout bandwidth = 100 kHz, echo spacing = 2700 μs, number of echo-shifts = 2 (effective echo spacing = 1350 μs, and effective number of echoes = 120). The total data acquisition time was 24.2 minutes with four averages. Other imaging parameters such as FOV and excitation volume were the same as those of the CSI data. A ΔB_0 map with the same imaging parameters as the phantom experiment, along with two anatomical images with T_1 ($T_R/T_E = 1000/30$ ms) and T_2 ($T_R/T_E = 1000/130$ ms) contrast were also obtained for ΔB_0 correction and SPICE image reconstruction.

The fat and lipid signals were removed from the CSI and EPSI data as described in [16]. After the removal of nuisance signals, the temporal subspace was estimated from the weighted ℓ_2 norm regularized ΔB_0 corrected reconstruction (on a 64×64 grid) of the CSI data. The estimated subspace was

then used to compute the spatial coefficients from the high-resolution EPSI data according to Eq. (3.11); a weighted ℓ_2 regularization term $\|\mathbf{W}\boldsymbol{U}\|_F^2$ with weights computed from the anatomical images was used.

To illustrate the usefulness of subspace-based MRSI we compared the SPICE reconstruction to a typical DFT-based reconstruction from CSI data. Figure 5.10 shows the NAA peak integrals of the minimum norm reconstruction of the CSI data and the SPICE reconstruction of the data. The peak integral distribution of the SPICE reconstruction contains much higher-resolution features, in particular the ventricles are much more clearly defined in Fig. 5.10d than they are in Fig. 5.10c. Figure 5.10e provides an example spectrum from the SPICE reconstruction showing that the gain in spatial resolution is made without sacrificing spectral quality. The possibility of increased resolution without the loss of spectral quality is made possible because the SPICE reconstruction takes advantage of the PS property in both data acquisition and reconstruction, greatly reducing the number of degrees of freedom of the reconstruction problem. Finally, we note that the time used to acquire both the CSI and EPSI data used in the SPICE reconstruction was 39.6 minutes. The time needed to acquire an equivalent resolution (112×112 gird size) CSI data set would be approximately 5.5 hours, hence the SPICE framework provides an acceleration factor of about 8.

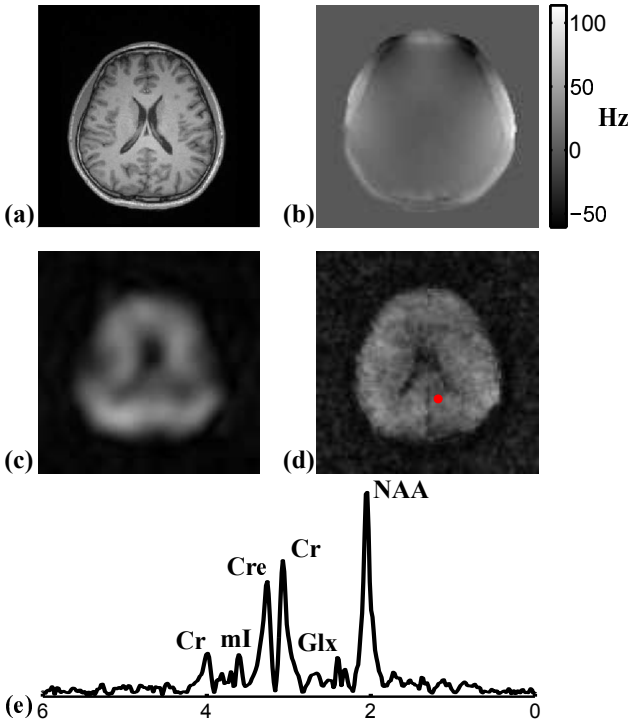

Figure 5.10: SPICE reconstruction results of *in vivo* data. (a) Anatomical reference image. (b) Estimated ΔB_0 map in Hz. (c) NAA peak integral from the minimum norm reconstruction of the CSI data. (d) NAA peak integral from the SPICE reconstruction. (e) Selected spectra from the SPICE reconstruction at the location indicated by the red dot in (d). The x-axis denotes chemical shift in ppm.

CHAPTER 6

CONCLUSIONS

The ability of MRSI to non-invasively image chemical distributions within an object makes it an ideal tool for studying biological systems. Unlike MRI, which has had an incredibly powerful impact on the fields of biology and medicine, MRSI has yet to have this level of impact due to the method's inherently poor trade-off between speed, resolution, and SNR.

Recently, subspace-based imaging methods for MRSI have been proposed which enable accelerated acquisition through use of the PS model. By incorporating the low-rank properties guaranteed by this model into the design of advanced data acquisition strategies and image reconstruction algorithms, subspace-based methods, such as SPICE, provide high-SNR, high-resolution images from sparsely sampled data.

A key ingredient in these methods, is the accurate determination of the temporal (spectral) subspace of the image (spatiospectral distribution function) from data with limited k-space coverage. Unfortunately, the effects of measurement noise and inhomogeneity in the magnetic field significantly increase the model order needed to accurately approximate the image with the PS model, thereby reducing the effectiveness of these methods. Motivated by this challenge, this thesis presented a method for accurately estimating the underlying low dimensional subspace from limited k-space coverage data acquired in the presence of field inhomogeneity and noise. Our method consists of a two-stage approach in which we first correct the data for the effects of field inhomogeneity using a regularized reconstruction-based method and then estimate the temporal subspace from the SVD of the corrected data.

We have compared several field correction methods and proposed novel ways for selecting regularization parameters as well as the dimension of the underlying subspace. Furthermore, we have demonstrated the effectiveness of the proposed method using results from simulated and experimentally acquired data. Results from the experimental data are consistent with the

observations made from the simulation studies which demonstrated the necessity of field correction prior to subspace estimation.

A key theme of subspace-based imaging methods as well as our field corrected reconstruction-based approach for subspace estimation is the utilization of *a priori* information. This appears in our field corrected reconstruction schemes via the introduction of a regularization term; however, after correction we rely on the SVD to provide our basis vector estimation. While this basis has desirable mathematical properties (e.g., orthonormality), they are not directly related to underlying spatiospectral distributions, which may limit our ability to incorporate further *a priori* information into the spatial coefficient estimation process. Within the SPICE framework, it is also possible to use temporal bases constructed based on the spectral distributions of the underlying chemicals imaged. How to estimate and use these types of physics-based basis functions in contrast to singular vector basis functions (constructed based on mathematical properties) should be considered in future work. These new subspace estimation methods, in combination with the development of new and exciting acquisition schemes may lead to truly practical MRSI which may in turn have broad impacts on the ways in which we study biology and medicine.

APPENDIX A

DERIVATIONS AND ALGORITHMS

A.1 Signal Measurement Equation

In this section we provide the proof of the signal measurement equation Eq. (2.6). Letting $\boldsymbol{J}_1$ and $\boldsymbol{E}_1$ be the current density and electric field inside of the receiver coil and $\boldsymbol{E}_2$ and $\boldsymbol{J}_2$ be the current density of the electric field in the object due to the time-varying $\boldsymbol{M}$, reciprocity theorem tells us that

$$\int_{V_\infty} \boldsymbol{E}_2 \cdot \boldsymbol{J}_l dv = \int_{V_\infty} \boldsymbol{E}_1 \cdot \boldsymbol{J}_2 dv, \tag{A.1}$$

where V_∞ can be taken as all of space. Since the current density due to $\boldsymbol{M}$ equals $\nabla \times \boldsymbol{M}$ and letting the current in the coil be denoted as I_1 and the voltage induced in the coil due to $\boldsymbol{M}$ be denoted as V_1 we have

$$I_1 \int_{\text{Coil}} \boldsymbol{E}_2 \cdot d\boldsymbol{l} = \int_{V_\infty} \boldsymbol{E}_1 \cdot \nabla \times \boldsymbol{M} dv, \tag{A.2}$$

where the first integral denotes integration over the receiver coil. Using the vector identity

$$\nabla \cdot (\boldsymbol{E}_1 \times \boldsymbol{M}) = \boldsymbol{M} \cdot \nabla \times \boldsymbol{E}_1 - \boldsymbol{E}_1 \cdot \nabla \times \boldsymbol{M}, \tag{A.3}$$

we can rewrite our previous equation as

$$I_1 V_1 = \int_{V_\infty} \boldsymbol{M} \cdot \nabla \times \boldsymbol{E}_1 dv - \int_{V_\infty} \nabla \cdot (\boldsymbol{E}_1 \times \boldsymbol{M})\, dv. \tag{A.4}$$

From Gauss' theorem the second integral evaluates to zero since both fields are zero at infinity. Then using Faraday's law of induction for time-harmonic

fields

$$\nabla \times \boldsymbol{E} = -i2\pi f \boldsymbol{B}, \tag{A.5}$$

we have

$$V_1 = -i\frac{2\pi f}{I_1}\int_{V_{\text{sample}}} \boldsymbol{M}\cdot\boldsymbol{B}_1 dv, \tag{A.6}$$

where the integration is performed over the sample volume.

A.2 The ADMM Algorithm

First, the augmented Lagrangian function for the problem in Eq. (4.13) can be written as

$$\begin{aligned} f(\boldsymbol{\rho}, \boldsymbol{A}, \boldsymbol{Z}) = &\parallel \mathbf{GB}\boldsymbol{\rho} - \boldsymbol{s} \parallel_2^2 \\ &+ \lambda\|\boldsymbol{A}\|_* + \frac{1}{2}\beta\|\boldsymbol{A} - \boldsymbol{C}(\boldsymbol{\rho})\|_F^2 \\ &+ \langle \boldsymbol{Z}, \boldsymbol{A} - \boldsymbol{C}(\boldsymbol{\rho})\rangle, \end{aligned} \tag{A.7}$$

where β is a chosen penalty parameter, $\boldsymbol{Z}$ is the Lagrange multiplier, and $\langle\cdot,\cdot\rangle$ denotes the matrix inner product defined as

$$\langle \boldsymbol{A}, \boldsymbol{B}\rangle := \mathrm{Tr}\left\{\boldsymbol{B}^H A\right\}. \tag{A.8}$$

The following alternating scheme was then used to minimize Eq. (A.7) with respect to $\boldsymbol{\rho}$, $\boldsymbol{A}$, and $\boldsymbol{Z}$:

1. For fixed $\boldsymbol{Z}_{i-1}$ and $\boldsymbol{A}_{i-1}$, we update $\boldsymbol{\rho}_i$ by solving

$$\begin{aligned} \boldsymbol{\rho}_i = &\arg\min_{\boldsymbol{\rho}} \parallel \mathbf{GB}\boldsymbol{\rho} - \boldsymbol{s} \parallel_2^2 \\ &+ \frac{1}{2}\beta_{i-1}\|\boldsymbol{A}_{i-1} - \boldsymbol{C}(\boldsymbol{\rho})\|_F^2 \\ &+ \langle \boldsymbol{Z}_{i-1}, \boldsymbol{A}_{i-1} - \boldsymbol{C}(\boldsymbol{\rho})\rangle \\ = &\arg\min_{\boldsymbol{\rho}} \parallel \mathbf{GB}\boldsymbol{\rho} - \boldsymbol{s} \parallel_2^2 \\ &+ \frac{1}{2}\beta_{i-1}\|\boldsymbol{C}(\boldsymbol{\rho}) - \boldsymbol{A}_{i-1} - \frac{\boldsymbol{Z}_{i-1}}{\beta_{i-1}}\|_F^2, \end{aligned} \tag{A.9}$$

which is equivalent to solving the following linear system of equations

$$\left(\mathbf{B}^H\mathbf{G}^H\mathbf{G}\mathbf{B}+\frac{1}{2}\beta_{i-1}\right)\boldsymbol{\rho}_i = \mathbf{B}^H\mathbf{G}^H\boldsymbol{s}+\frac{1}{2}\operatorname{vec}\left\{\beta_{i-1}\boldsymbol{A}_{i-1}+\boldsymbol{Z}_{i-1}\right\}. \tag{A.10}$$

2. For fixed $\boldsymbol{\rho}_i$ and $\boldsymbol{Z}_{i-1}$, we update $\boldsymbol{A}_i$ by solving

$$\begin{aligned}\boldsymbol{A}_i = &\arg\min_{\boldsymbol{A}}\lambda\|\boldsymbol{A}\|_* \\ &+\frac{1}{2}\beta_{i-1}\|\boldsymbol{A}-\boldsymbol{C}(\boldsymbol{\rho}_i)\|_F^2 \\ &+\langle\boldsymbol{Z}_{i-1},\boldsymbol{A}-\boldsymbol{C}(\boldsymbol{\rho}_i)\rangle \\ = &\arg\min_{\boldsymbol{A}}\lambda\|\boldsymbol{A}\|_* \\ &+\frac{1}{2}\beta_{i-1}\|\boldsymbol{C}(\boldsymbol{\rho}_i)-\frac{\boldsymbol{Z}_{i-1}}{\beta_{i-1}}-\boldsymbol{A}\|_F^2,\end{aligned} \tag{A.11}$$

which has a closed-form solution as [65]

$$\boldsymbol{A}_i = \boldsymbol{P}\ \operatorname{diag}\{s_r\}\ \boldsymbol{Q}, \tag{A.12}$$

where

$$s_r = \operatorname{sign}\{\sigma_r\}\max\left\{|\sigma_r|-\frac{\lambda}{\beta_{i-1}},0\right\}, \tag{A.13}$$

and

$$\boldsymbol{C}(\boldsymbol{\rho}_i)-\frac{\boldsymbol{Z}_{i-1}}{\beta_{i-1}} = \boldsymbol{P}\ \operatorname{diag}\{\sigma_r\}\ \boldsymbol{Q}. \tag{A.14}$$

3. For fixed $\boldsymbol{\rho}_i$ and $\boldsymbol{A}_i$, we update the Lagrange multiplier according to

$$\boldsymbol{Z}_i = \boldsymbol{Z}_{i-1}+\beta_{i-1}\left(\boldsymbol{A}_i-\boldsymbol{C}(\boldsymbol{\rho}_i)\right) \tag{A.15}$$

and update the penalty parameter according to

$$\beta_i = \alpha\beta_{i-1}, \tag{A.16}$$

where α is a predetermined penalty parameter greater than one.

4. We repeat steps 1-3 until the following convergence criteria is met

$$\frac{\|\boldsymbol{\rho}_i - \boldsymbol{\rho}_{i-1}\|_2}{\|\boldsymbol{\rho}_{i-1}\|_2} < \epsilon \qquad \text{for } \epsilon > 0. \tag{A.17}$$

In this work we solved Eq. (A.10) using a linear conjugate gradient descent method with the same convergence criteria as for step 4 of the overall scheme. Experimentation with the values of ϵ, β_0 and α revealed that good results and reasonable convergence rates could be met by setting $\epsilon = 10^{-5}$, $\beta_0 = 1$ and $\alpha = 1.2$. We initialized both $\boldsymbol{A}$ and $\boldsymbol{Z}$ as zero matrices. Figure A.1 shows the effect of a good choice of α on the convergence of the algorithm.

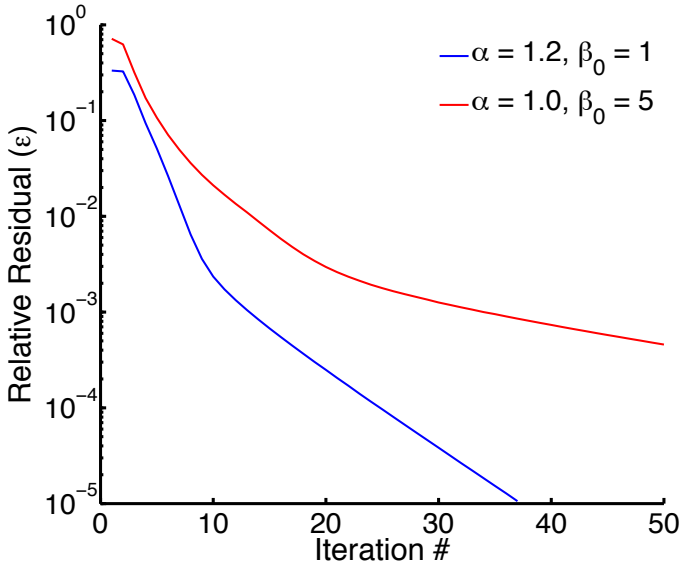

Figure A.1: Convergence of the nuclear norm regularized reconstruction of $\mathcal{D}_1$ data with (blue) and without (red) continuation of β. In the red curve, β_0 was chosen empirically for convergence. The data in the reconstruction was the 16×16 data with good SNR and ΔB_0 generated from the numerical phantom.

For the hybrid method combining the nuclear norm and weighted ℓ_2 regularization functionals, the augmented Lagrangian function is given by

$$\begin{aligned} f(\boldsymbol{\rho}, \boldsymbol{A}, \boldsymbol{Z}) = &\parallel \mathbf{GB}\boldsymbol{\rho} - \boldsymbol{s} \parallel_2^2 \\ &+ \frac{1}{2}\mu \boldsymbol{\rho}^H \mathbf{D}^T \mathbf{W} \mathbf{D} \boldsymbol{\rho} \\ &+ \lambda \|\boldsymbol{A}\|_* + \frac{1}{2}\beta \|\boldsymbol{A} - \boldsymbol{C}(\boldsymbol{\rho})\|_F^2 \\ &+ \langle \boldsymbol{Z}, \boldsymbol{A} - \boldsymbol{C}(\boldsymbol{\rho}) \rangle, \end{aligned} \tag{A.18}$$

and in the first step, the system of equations to be solved for is instead given by

$$\begin{aligned}\left(\mathbf{B}^H\mathbf{G}^H\mathbf{G}\mathbf{B}+\frac{1}{2}\mu\mathbf{D}^T\mathbf{W}\mathbf{D}+\frac{1}{2}\beta_{i-1}\right)\boldsymbol{\rho}_i \\ =\mathbf{B}^H\mathbf{G}^H\boldsymbol{s}+\frac{1}{2}\operatorname{vec}\left\{\beta_{i-1}\boldsymbol{A}_{i-1}+\boldsymbol{Z}_{i-1}\right\}.\end{aligned} \tag{A.19}$$

Although, we do not present any results for this method, it was found that the this hybrid method did not yield significantly better results.

REFERENCES

[1] E. M. Purcell, H. C. Torrey, and R. V. Pound, "Resonance absorption by nuclear magnetic moments in a solid," *Phys. Rev.*, vol. 69, pp. 37 – 38, 1946.

[2] F. Bloch, W. W. Hansen, and M. Packard, "Nuclear induction," *Phys. Rev.*, vol. 69, p. 127, 1946.

[3] F. Bloch, "Nuclear induction," *Phys. Rev.*, vol. 70, pp. 460 – 474, 1946.

[4] P. C. Lauterbur, D. M. Kramer, W. V. House, and C.-N. Chen, "Zeugmatographic high resolution nuclear magnetic resonance spectroscopy: Images of chemical inhomogeneity within macroscopic objects," *J. Amer. Chem. Soc.*, vol. 97, pp. 6866 – 6868, 1975.

[5] T. R. Brown, B. M. Kincaid, and K. Ugurbil, "NMR chemical shift imaging in three dimensions," *Proc. Natl. Acad. Sci.*, vol. 29, pp. 3523 – 2526, 1982.

[6] A. A. Maudsley, S. K. Hilal, W. H. Perman, and H. E. Simon, "Spatially resolved high resolution spectroscopy by 'four-dimensional' NMR," *J. Magn. Reson.*, vol. 51, pp. 147 – 152, 1983.

[7] P. Mansfield, "Spatial mapping of the chemical shift in NMR," *Magn. Reson. Med.*, vol. 1, pp. 370 – 386, 1983.

[8] P. C. Lauterbur, D. N. Levin, and R. B. Marr, "Theory and simulation of NMR spectroscopic imaging and field plotting by projection reconstruction involving an intrinsic frequency dimension," *J. Magn. Reson.*, vol. 59, pp. 536 – 541, 1984.

[9] J. Kurhanewicz, D. B. Vigneron, and S. J. Nelson, "Three-dimensional magnetic resonance spectroscopic imaging of brain and prostate cancer," *Neoplasia*, vol. 2, pp. 166 – 189, 2000.

[10] S. J. Nelson, "Assessment of therapeutic response and treatment planning for brain tumors using metabolic and physiological MRI," *NMR Biomed.*, vol. 24, pp. 734 – 749, 2011.

[11] B. Hamans, A. C. Navis, A. Wright, P. Wesseling, A. Heerschap, and W. Leenders, "Multivoxel 1H MR spectroscopy is superior to contrast-enhanced MRI for response assessment after anti-angiogenic treatment of orthotopic human glioma xenografts and provides handles for metabolic targeting," *Neuro-Oncology*, vol. 15, pp. 1615 – 1624, 2013.

[12] J. M. Schott, C. Frost, D. G. MacManus, F. Ibrahim, A. D. Waldman, and N. C. Fox, "Short echo time proton magnetic resonance spectroscopy in Alzheimer's disease: A longitudinal multiple time point study," *Brain*, vol. 133, pp. 3315 – 3322, 2010.

[13] D. T. Chard, C. M. Griffin, M. A. McLean, P. Kapeller, R. Kapoor, A. J. Thompson, and D. H. Miller, "Brain metabolite changes in cortical grey and normal appearing white matter in clinically early relapsing-remitting multiple sclerosis," *Brain*, vol. 125, pp. 2342 – 2352, 2002.

[14] F. Lam and Z.-P. Liang, "A subspace approach to high–resolution spectroscopic imaging," *Magn. Reson. Med.*, vol. 71, pp. 1349 – 1357, 2014.

[15] F. Lam, C. Ma, B. Clifford, C. L. Johnson, and Z.-P. Liang, "High-resolution 1H-MRSI of the brain using SPICE: Data acquisition and image reconstruction," *Magn. Reson. Med.*, 2015.

[16] C. Ma, F. Lam, C. L. Johnson, and Z.-P. Liang, "Removal of nuisance signals from limited and sparse 1H MRSI data using a union-of-subspaces model," *Magn. Reson. Med.*, vol. 75, pp. 488 – 497, 2016.

[17] C. Ma, F. Lam, Q. Ning, C. L. Johnson, and Z.-P. Liang, "High-resolution 1H-MRSI of the brain using short-TE SPICE," *Magn. Reson. Med.*, 2016.

[18] Z.-P. Liang and P. C. Lauterbur, *Principles of Magnetic Resonance Imaging: A Signal Processing Perspective*. IEEE Press, 2000.

[19] C. P. Slichter, *Principles of Magnetic Resonance*, 3rd ed. Springer-Verlag, 1992.

[20] R. A. de Graaf, *In Vivo NMR Spectroscopy*. John Wiley & Sons, Ltd, 2007.

[21] A. Haase, J. Frahm, W. Hnicke, and D. Matthaei, "1H NMR chemical shift selective (CHESS) imaging," *Phys. Med. Biol.*, vol. 30, pp. 341 – 344, 1985.

[22] D. M. Spielman, J. M. Pauly, A. Macovski, G. H. Glover, and D. R. Enzmann, "Lipid-suppressed single-and multisection proton spectroscopic imaging of the human brain," *Journal of Magnetic Resonance Imaging*, vol. 2, pp. 253 – 262, 1992.

[23] J. H. Duyn, J. Gillen, G. Sobering, P. C. van Zijl, and C. T. Moonen, "Multisection proton MR spectroscopic imaging of the brain," *Radiology*, vol. 188, pp. 277 – 282, 1993.

[24] R. Ogg, R. Kingsley, and J. Taylor, "WET, a T1- and B1-insensitive water-suppression method for in vivo localized 1H NMR spectroscopy," *J. Magn. Reson. B*, vol. 104, pp. 1 – 10, 1994.

[25] C. I. Haupt, N. Schuff, M. W. Weiner, and A. A. Maudsley, "Removal of lipid artifacts in 1H spectroscopic imaging by data extrapolation," *Magn. Reson. Med.*, vol. 35, pp. 678 – 687, 1996.

[26] J. H. Duyn, J. Gillen, G. Sobering, P. C. van Zijl, and C. T. Moonen, "Truncation artifact reduction in spectroscopic imaging using a dual-density spiral k-space trajectory," *Magn. Reson. Imag.*, vol. 20, pp. 743 – 757, 2002.

[27] S. Posse, G. Tedeschi, R. Risinger, R. Ogg, and D. L. Bihan, "High speed 1H spectroscopic imaging in human brain by echo planar spatial-spectral encoding," *Magn. Reson. Med.*, vol. 33, pp. 34 – 40, 1995.

[28] J. B. Johnson, "Thermal agitation of electricity in conductors," *Phys. Rev.*, vol. 32, pp. 97 – 109, 1928.

[29] H. Nyquist, "Thermal agitation of electric charge in conductors," *Phys. Rev.*, vol. 32, pp. 110 – 113, 1928.

[30] R. Pohmann, M. von Kienlin, and A. Haase, "Theoretical evaluation and comparison of fast chemical shift imaging methods," *J. Magn. Reson.*, vol. 129, pp. 145 – 160, 1997.

[31] S. Posse, G. Tedeschi, R. Risinger, R. Ogg, and D. L. Bihan, "High speed 1H spectroscopic imaging in human brain by echo planar spatial-spectral encoding," *Magn. Reson. Med.*, vol. 33, pp. 34 – 40, 1995.

[32] E. Adalsteinsson, P. Irarrazabal, S. Topp, C. Meyer, A. Macovski, and D. M. Spielman, "Volumetric spectroscopic imaging with spiral-based k-space trajectories," *Magn. Reson. Med.*, vol. 39, pp. 889 – 898, 1998.

[33] F.-H. Lin, S.-Y. Tsai, R. Otazo, A. Caprihan, L. L. Wald, J. W. Belliveau, and S. Posse, "Sensitivity-encoded (SENSE) proton echo-planar spectroscopic imaging (PEPSI) in the human brain," *Magn. Reson. Med.*, vol. 57, pp. 249 – 257, 2007.

[34] X. Hu, D. N. Levin, P. C. Lauterbur, and T. Spraggins, "SLIM: Spectral localization by imaging," *Magn. Reson. Med.*, vol. 8, pp. 314 – 322, 1988.

[35] Z.-P. Liang and P. C. Lauterbur, "A generalized series approach to MR spectroscopic imaging," *IEEE Trans. Med. Imag.*, vol. 10, pp. 132 – 137, 1991.

[36] M. Jacob, X. Zhu, A. Ebel, N. Schuff, and Z.-P. Liang, "Improved model-based magnetic resonance spectroscopic imaging," *IEEE Trans. Med. Imag.*, vol. 26, pp. 1305 – 1318, 2007.

[37] R. Eslami and M. Jacob, "Robust reconstruction of MRSI data using a sparse spectral model and high resolution MRI priors," *IEEE Trans. Med. Imag.*, vol. 29, pp. 1297 – 1309, 2010.

[38] J. Kornak, K. Young, B. J. Soher, and A. A. Maudsley, "Bayesian k-space-time reconstruction of MR spectroscopic imaging for enhanced resolution," *IEEE Trans. Med. Imag.*, vol. 29, pp. 1333 – 1350, 2010.

[39] I. Chatnuntawech, B. Bilgic, and E. Adalsteinsson, "Undersampled spectroscopic imaging with model-based reconstruction," in *Proc. Int. Symp. Magn. Reson. Med.*, Salt Lake City, UT, USA, 2013, p. 3960.

[40] Y. Zhang, R. E. Gabr, M. Schar, R. G. Weiss, and P. A. Bottomley, "Magnetic resonance spectroscopy with linear algebraic modeling (SLAM) for higher speed and sensitivity," *J. Magn. Reson.*, vol. 218, pp. 66 – 76, 2012.

[41] J. Kasten, F. Lazeyras, and D. Van De Ville, "Data-driven MRSI spectral localization via low-rank component analysis," *IEEE Trans. Med. Imag.*, 2013.

[42] Z.-P. Liang, "Spatiotemporal imaging with partially separable functions," in *Proc. IEEE Int. Symp. on Biomed. Imag.*, Arlington, VA, USA, 2007, pp. 988 – 991.

[43] J. P. Haldar and Z.-P. Liang, "Spatiotemporal imaging with partially separable functions: A matrix recovery approach," in *Proc. IEEE Int. Symp. on Biomed. Imag.*, Rotterdam, Netherlands, 2010, pp. 716 – 719.

[44] H. M. Nguyen, X. Peng, M. N. Do, and Z.-P. Liang, "Denoising MR spectroscopic imaging data with low-rank approximations," *IEEE Trans. Biomed. Eng.*, vol. 60, pp. 78 – 89, 2013.

[45] B. Zhao, J. Haldar, A. Christodoulou, and Z.-P. Liang, "Image reconstruction from highly undersampled ($\mathbf{k}$, t) -space data with joint partial separability and sparsity constraints," *IEEE Trans. Med. Imag.*, vol. 31, pp. 1809 – 1820, Sept 2012.

[46] A. W. Naylor and G. R. Sell, *Linear Operator Theory in Engineering and Science*, 2nd ed. Springer-Verlag, 1982.

[47] X. Peng, H. Nguyen, J. Haldar, D. Hernando, X.-P. Wang, and Z.-P. Liang, "Correction of field inhomogeneity effects on limited k-space MRSI data using anatomical constraints," in *Conf. Proc. IEEE Eng. Med. Biol. Soc.*, Buenos Aires, Argentina, 2010, pp. 883 – 886.

[48] J. P. Haldar, D. Hernando, S. K. Song, and Z.-P. Liang, "Anatomically constrained reconstruction from noisy data," *Magn. Reson. Med.*, vol. 59, pp. 810 – 818, 2008.

[49] E. J. Candès, X. Li, Y. Ma, and J. Wright, "Robust principal component analysis?" *J. ACM*, vol. 58, pp. 1 – 37, 2011.

[50] Y. Liu, C. Ma, B. Clifford, F. Lam, C. L. Johnson, and Z.-P. Liang, "Improved low-rank filtering of magnetic resonance spectroscopic imaging data corrupted by noise and B0 field inhomogeneity," *IEEE Trans. Biomed. Eng.*, vol. 63, pp. 841 – 849, 2016.

[51] Z. Lin, M. Chen, and Y. Ma, "The augmented Lagrange multiplier method for exact recovery of corrupted low-rank matrices," http://arxiv.org/abs/1009.5055, 2010.

[52] S. Boyd, N. Parikh, E. Chu, B. Peleato, and J. Eckstein, "Distributed optimization and statistical learning via the alternating direction method of multipliers," *Found. Trends. Mach. Learn.*, vol. 3, pp. 1 – 122, 2011.

[53] C. R. Vogel, *Computational Methods for Inverse Problems*. Philadelphia, PA: SIAM, 2002.

[54] V. A. Marenko and L. A. Pastur, "Distribution of eigenvalues for some sets of random matrices," *Math USSR Sbornik*, vol. 1, p. 457, 1967.

[55] A. Edelman, "Eigenvalues and condition numbers of random matrices," *SIAM J. Matrix Anal. Appl.*, vol. 9, pp. 543 – 560, 1988.

[56] Y. Ding, Y.-C. Chung, and O. P. Simonetti, "A method to assess spatially variant noise in dynamic MR image series," *Magn. Reson. Med.*, vol. 63, pp. 782 – 789, 2010.

[57] B. J. Soher, K. Young, A. Bernstein, Z. Aygula, and A. A. Maudsley, "GAVA: Spectral simulation for in vivo MRS applications," *J. Magn. Reson.*, vol. 185, pp. 291 – 299, 2007.

[58] J. Miao and A. Ben-Israel, "On principal angles between subspaces in $\mathbb{R}^n$," *Linear Algebra Appl.*, vol. 171, pp. 81 – 98, 1992.

[59] H. Gunawan, O. Neswan, and W. Setya-Budhi, "A formula for angles between subspaces of inner product spaces," *Beitr. Algebra. Geom.*, vol. 46, pp. 311 – 320, 2005.

[60] R. Eslami and M. Jacob, "Correction of B0 inhomogeneity distortion in magnetic resonance spectroscopic imaging," in *Proc. IEEE Int. Conf. Acoust. Speech Signal Process.*, 2009, pp. 405 – 408.

[61] M. E. Halse and P. T. Callaghan, "Imaged deconvolution: A method for extracting high-resolution NMR spectra from inhomogeneous fields," *J. Magn. Reson.*, vol. 185, pp. 130 – 137, 2007.

[62] Z. Dong and B. S. Peterson, "Spectral resolution amelioration by deconvolution (SPREAD) in mr spectroscopic imaging," *J. Magn. Reson. Imag.*, vol. 29, pp. 1395 – 1405, 2009.

[63] H. Barkhuysen, R. de Beer, and D. van Ormondt, "Improved algorithm for noniterative time-domain model fitting to exponentially damped magnetic resonance signals," *J. Magn. Reson.*, vol. 73, pp. 553 – 557, 1987.

[64] M. Bydder, G. Hamilton, T. Yokoo, and C. B. Sirlin, "Optimal phased-array combination for spectroscopy," *Magn. Reson. Imag.*, vol. 26, pp. 847 – 850, 2008.

[65] J.-F. Cai, E. J. Candès, and Z. Shen, "A singular value thresholding algorithm for matrix completion," *SIAM J. Optim.*, vol. 20, pp. 1956 – 1982, 2010.